Quantitative assessment of mitochondrial morphology relevant for studies on cellular health and environmental toxicity

Sophie Charrasse, Titouan Poquillon, Charlotte Saint-Omer, Manuela Pastore, Benoit Bordignon, Richard E Frye, Christelle Reynes, Victor Racine, Abdel Aouacheria

Quantitative assessment of mitochondrial morphology relevant for studies on cellular health and environmental toxicity

Sophie Charrasse[1], Titouan Poquillon[1, 2], Charlotte Saint-Omer[1], Manuela Pastore[3], Benoit Bordignon[4], Richard E Frye[5], Christelle Reynes[3,6], Victor Racine[2] and Abdel Aouacheria[1,†]

[1] Institut des Sciences de l'Evolution de Montpellier (ISEM, UMR 5554, CNRS/UM/IRD/EPHE), Université de Montpellier, Montpellier, France

[2] QuantaCell SAS, Hôpital Saint Eloi, IRMB, 80 avenue Augustin Fliche, 34090 Montpellier, France

[3] STATABIO BioCampus, Univ. Montpellier, CNRS, INSERM, Montpellier, France

[4] MRI, Montpellier Ressources Imagerie, BioCampus, University of Montpellier, CNRS, INSERM, Montpellier, France

[5] Autism Discovery and Treatment Foundation, Phoenix AZ, USA

[6] IGF, Univ. Montpellier, CNRS, INSERM, Montpellier, France

Corresponding author:

Abdel Aouacheria[†]

Institut des Sciences de l'Evolution de Montpellier (ISEM, UMR 5554, CNRS/UM/IRD/EPHE), Université de Montpellier, Montpellier, France

Email address: abdel.aouacheria@umontpellier.fr

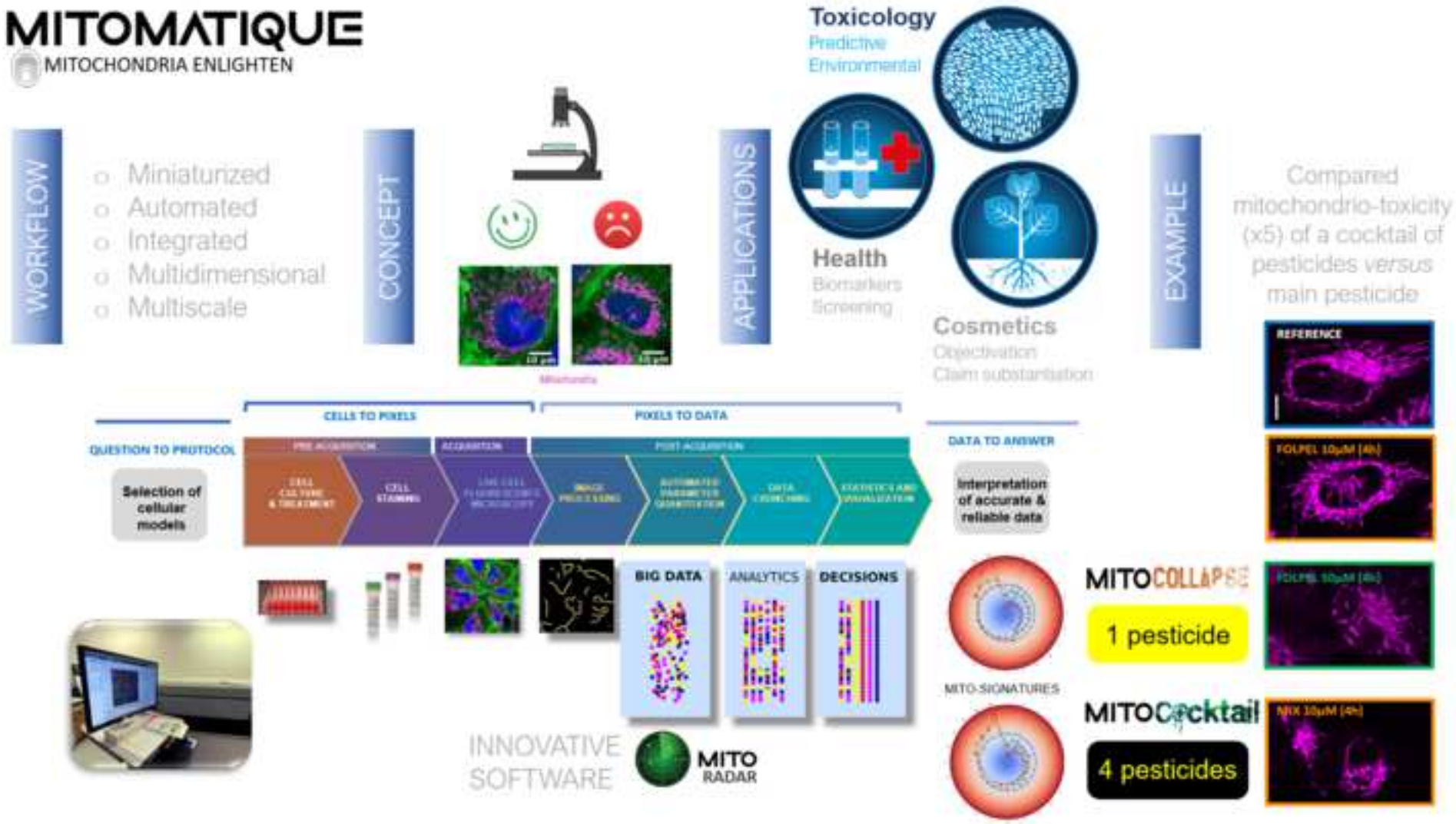

Abstract (250 words)

Mitochondria are essential organelles that play crucial roles in cellular energy metabolism, calcium signaling and apoptosis. Their importance in tissue homeostasis and stress responses, combined to their ability to transition between various structural and functional states, make them excellent organelles for monitoring cellular health. Quantitative assessment of mitochondrial morphology can therefore provide valuable insights into environmentally-induced cell damage.

High-content screening (HCS) provides a powerful tool for analyzing organelles and cellular substructures. We developed a fully automated and miniaturized HCS wet-plus-dry pipeline (MITOMATICS) exploiting mitochondrial morphology as a marker for monitoring cellular health or damage. MITOMATICS uses an in-house, proprietary software (MitoRadar) to enable fast, exhaustive and cost-effective analysis of mitochondrial morphology and its inherent diversity in live cells.

We applied our pipeline and big data analytics software to assess the mitotoxicity of selected chemicals, using the mitochondrial uncoupler CCCP as an internal control. Six different pesticides (inhibiting complexes I, II and III of the mitochondrial respiratory chain) were tested as individual compounds and five other pesticides present locally in Occitanie (Southern France) were assessed in combination to determine acute mitotoxicity. Our results show that the assayed pesticides exhibit specific signatures when used as single compounds or chemical mixtures and that they function synergistically to impact mitochondrial architecture.

Study of environment-induced mitochondrial damage has the potential to open new fields in mechanistic toxicology, currently underexplored by regulatory toxicology and exposome research. Such exploration could inform health policy guidelines and foster pharmacological intervention, water, air and soil pollution control and food safety.

Keywords

Mitochondria; quantitative imaging; cellular stress ; confocal microscopy ; high content analysis; live-cell imaging; environmental health; pesticides.

Short title

Quantitative imaging and phenotyping of mitochondria for toxicity studies.

1. Introduction

Mitochondria play a vital role in ATP production and in many critical cellular processes (1,2). Mitochondrial markers are among the first to change upon homeostasis disruption, such as when cells are exposed to environmental stress (3–5) (e.g. toxicants), and during disease (6,7) and aging (8). By sensing and responding to changes in the cellular environment, mitochondria orchestrate adaptive responses that extends well over cellular boundaries to impact tissue, organ and ultimately organism physiology (9). The importance of mitochondria in tissue homeostasis, stress responses and diseases, combined to their ability to transition between various structural and functional states, make them excellent organelles for monitoring cell health (10).

Healthy mitochondria are usually mobile, tubular and interconnected, whereas cells under stress or entering apoptosis often display swollen or fragmented mitochondria, marked by concurrent disruption of metabolism and excess production of reactive oxygen species (ROS) (11). Mitochondrial change in shape and size depending on their functional status, for example going though cycles of fission and fusion to improve mitochondrial quality (12). Thus, mitochondrial morphological phenotypes are complex and heterogeneous. The morphological diversity of this highly dynamic organelle varies from small punctate structures to well-developed reticular networks with numerous intermediate states in-between. To define or classify mitochondrial (network) architectures, only a few terms are usually used, such as *short*, *long*, *fragmented*, *interconnected*, *tubular*, *ramified*, *compacted*, *aggregated*, *dislocated*, *fissioned* or *hyperfused* (13–15). These terms are often used in an operator-dependent, subjective way.

In recent years, to address the challenge of describing this inherent mitochondrial diversity more objectively, several approaches which apply image processing algorithms and morphometric methods have been developed (16–18), providing valuable insights into tissue physiology, pathology and damage (19–21). However, most of these programs are difficult to utilize in standard biology laboratories since they require extensively trained staff and only handle the morphological computation steps, with no visual display, statistical analysis or decision-making support. In most cases, only a limited number of cells or conditions are analyzed with such software, creating ambiguity about the robustness of the obtained data and ultimately as to the true utility of such software.

Over the last few years, we developed a sophisticated and innovative pipeline (MITOMATICS) exploiting mitochondrial morphology as a marker for monitoring cellular health or damage. MITOMATICS uses computerized methods to enable accurate, fast and cost-effective analysis of mitochondrial shape and network architecture from confocal fluorescent images acquired from cultured living cells. Three successive versions of this in-house, proprietary software were produced: MitoShape (2 shape descriptors) (22), MitoTouch (31 descriptors) (Charrasse et al., submitted) and the here within described MitoRadar (104 shape descriptors). This software is easy to use and does not require any special skills in computer science or image processing. In contrast to previous versions, numerous parameters have been added to provide a multiscale analysis of the mitochondrial component (from solitary mitochondria to mitochondrial clusters present within single cells or in a cell population) and the segmentation step is now performed by deep learning, enhancing image quality and enabling accurate analysis. As a result, MitoRadar generates specific 'mito-signatures', some of which signal cell safety whereas others may provide early predictors of cell danger. In the present study, we applied MitoRadar in the context of predictive and environmental toxicology by assessing mitochondrial architecture in live human cells exposed to specific chemicals, including pesticides used alone or in combination.

2. Materials and methods

2.1.1. Chemicals

Dimethyl sulfoxide (DMSO; CAS number 67-68-5), Carbonyl cyanide m-chlorophenyl hydrazone (CCCP; CAS number 555-60-2), Rotenone (CAS number 83-79-4), Antimycine A (CAS number 1397-94-0), Mitochondrial Division Inhibitor MDIVI-1 (CAS number 338967-87-6), Mitochondrial Fusion Promoter M1 (CAS number 219315-22-7), Fenpyroximate (CAS number 134098-61-6), Pyridaben (CAS number 96489-71-3), Mepronil (CAS number 55814-41-0), Thifluzamide (CAS number 130000-40-7), Azoxystrobin (CAS number 131860-33-8), Pyraclostrobin (CAS number 175013-18-0), Folpet (CAS number 133-07-3), Pendimathaline, Chlorpyriphos-Methyl (CAS number 5598-13-0), Lindane

(CAS number 58-89-9), Cyprodinil (CAS number 121552-61-2) were purchased from Sigma Aldrich. Stock solutions between 2 and 100 mM were made in DMSO and stored at -20°C until use. Treatment solutions were prepared freshly for each experiment with a final concentration of DMSO below 0.5 % (v/v) in culture medium.

2.1.2. Cell culture and treatments

A549 (CCL-185), RPE-1 (CRL-4000), U2OS (CRL-3455), Hs68 (CRL-1635), MDA-MB-231 (HTB-26), THLE-3 (CRL-11233), HK-2 (CRL-2190) and BEAS-2B (CRL-9482) cell lines were purchased from ATCC (American Type Culture Collection, LGC, Germany) and cultured in a 5% CO_2 atmosphere at 37°C according to ATCC recommendations. To increase the susceptibility of cells to mitochondrial toxicants, culture medium was replaced by freshly prepared glucose-free medium supplemented with 10mM galactose. For treatment, indicated concentrations of chemicals were added to the culture medium. LD50 was determined by counting nuclei 24h after drug exposure. Four biological replicates were performed for all experiments and each experiment was repeated at least 3 times. For the *MitoCocktail* experiments, the most prominent pesticides were tested at concentrations from 10 to 500µM and solutions were prepared according to a rule of conservative ratios, i.e., by mixing different pesticides with relative proportions (expressed in µM) based on the ATMO report (where pesticide concentrations are expressed as ng of substance per m^3 of air).

2.1.3. Cell staining and HCS Imaging

A total number of 20,000 to 40,000 cells were seeded onto 96-well black polystyrene microplates (CLS3603, Corning®) 24 to 48h prior conducting experiments. Mitochondrial morphology was examined after staining with 250 nM MitoTracker Deep Red FM (M22426) diluted in phenol red-free culture medium in presence of 2.5 µg/mL Hoechst 33342 (H21492) for 30 min at 37°C. Cells were then washed twice with PBS and labelled with 6.25 µg/mL CellMask Green Plasma Membrane Stain (C37608) for 5 min at 37°C. All these vital dyes were purchased from Thermofisher Scientific (Life Technologies SAS, Courtaboeuf, France). Mitochondrial network, nuclei and membranes of live cells were imaged using the Opera Phenix® High-Content Screening System (PerkinElmer Inc.). Confocal

image acquisition (spinning disk) was performed using a 63x water immersion lens (1.15NA LD C-Apochromat) and 5 fields were imaged per well. Automated image capture on a 16bit sCMOS camera (pixel 6.5 µm) using 640 nm/488 nm/405 nm lasers in the indicated order, with Phenix emission filters 650-760 nm/500-550 nm/435-550 nm, has been optimized to provide high image quality and resolution. In particular, laser power and exposure time were adjusted to maximize signal without saturation and to minimize photobleaching and background noise (20% power, 100 ms for the far-red channel, 80% power, 500 ms for the green channel and 100%, 200 ms for the blue channel).

2.1.4. Quantification of mitochondrial parameters using MitoRadar

As described below, the MitoRadar software (APP deposit number: IDDN.FR.001.470036 .000.S.P.2022.000.31235) consists of several modules designed for data handling, data processing, detection and comprehensive analysis of mitochondrial changes in HCS imaging data.

2.1.5. Basic image import and processing

First, a loading module enables the import of fluorescence images from high-content imaging (HCI) microscopes. A plate module can be used to add experimental data information during the loading stage. A data handling module allows for the sorting of images and assignment of plate data, well data, and experimental data. It can also be used to add and update experimental data information at any time during the analysis process.

The segmentation module of MitoRadar uses deep learning and state-of-the-art image processing techniques to detect cells, nuclei and mitochondria in HCS images (Fig. S1 A) at various scales (Fig. S1 B). The MitoRadar segmentation technique utilizes a tri-channel fluorescence image input with different colors associated to nuclei, mitochondria and cytoplasm. In this study, 2160x2160 images were analyzed at a resolution of 94nm.pix-1 (Fig. S1 C panel a).

Next, both nucleus and cell channels undergo a normalization process between 0 and 1 utilizing a quantile normalization approach between quantile 1% and quantile 99%. A trained convolutional network (Cellpose uNet) (23,24) is applied to each channel to perform instance segmentation of cell and nuclei. The uNet produces a probability map and a gradient flow which enables the reconstruction

of object instances. This method was proven to be effective for cell segmentation of objects with irregular shapes (25–27). To reduce computation time, the images are down-sampled to 224 pixels before entering the neural network and are up-sampled post-analysis using nearest neighbors followed by a median filtering technique to smooth edges (Fig. S1 C panel b). The nuclei instances are then associated with cells utilizing a 1-to-1 association rule, with the greater intersection size used to resolve conflicts when necessary (Fig. S1 C panel c).

Due to variations in mitochondrial intensity between cells within the same field, mitochondrial segmentation is performed cell by cell following the segmentation of nuclei and cells. The corresponding bounding box within the mitochondrial channel is extracted for each cell, and the average intensity inside the cell mask is utilized for background noise removal. The intensities are normalized between 0 and 1 utilizing a quantile normalization approach between quantile 0% and quantile 99.9%. Next, a Gaussian difference threshold (sigma=0.9 µm, t=0.05) and a Laplacian of Gaussian threshold (sigma=0.9 µm, t=0) are applied to produce a mitochondrial mask for the cell. Clusters are defined as connected components on this mask (Fig. S1 C panel d) and are refined by removing small objects (size < 16 pixels or 0.13 µm²) followed by morphological closing. The skeletons of mitochondrial clusters are extracted utilizing Zhang's algorithm (28) (Fig. S1 C panel e). Finally, to detect each individual instance of mitochondria, a watershed approach is applied to mitochondrial intensities using the skeleton branches as seeds and the mitochondrial mask as the mask (Fig. S1 C panel f). Moreover, this segmentation module can be parallelized and utilizes the GPU for fast processing of a large number of images.

2.1.6.Automated parameter quantification with integrated statistics

After segmentation, pictures are declumped and a quantification module then collects 104 morphological, intensity and texture parameters (hereby referred to as 'morphological descriptors'; see Table S1 for the exhaustive list and further details) on cells, nuclei, mitochondria and mitochondrial clusters. These descriptors can be used to characterize various aspects of mitochondrial architecture, such as size, shape, density and organization within the cellular area. Note that the current version of the software does not normalize descriptor values based on the cell size. Finally, the analysis module

of MitoRadar allows users to make state-of-the-art statistical tests and plots on the resulting quantifications and to easily compare experimental conditions. This module also includes integrated linear discriminant analysis (LDA) and principal component analysis (PCA) for exploring multivariate effects and a specific MitoRadar plot to access both significance and amplitude information.

The MitoRadar analysis module can calculate a MitoScore based on a cross validation of the impact (difference with the basal condition) and number of all affected parameters. First, a hierarchical clustering is applied to remove redundancies among descriptors. Then, 20 LDA models are trained on 50% fold random samples of the data to differentiate between the control and the trial conditions. These are then tested on the complementary folds using the average balanced accuracy between all LDA models as a score showing how easily a ML algorithm can discriminate between control and trial. The top 15 significant uncorrelated descriptors that discriminate the compared conditions are then shown in a MitoRadar plot and a slider is placed along a heat color scale, leading to the delineation of five distinct categories (*No effect*, *Limited / Substantial / Measurable* or *Large overall effect*) (Fig.1).

3. Results

3.1.1. Design of the MITOMATICS workflow

Quantitative imaging of cellular structures and substructures like mitochondria requires rethinking low-throughput experimental procedures to include the use of multi-well plates (rather than tissue culture petri dishes or small imaging chambers), live cell techniques (instead of fixed-cell imaging methods), random imaging of multiple fields (rather than operator-dependent monitoring of only one chosen microscope field encompassing multiple cells), databases of high-quality, classified images (rather than production of a limited number of acquired images), automated digital image processing (instead of manual counting) and rapid, massive data gathering, analysis and visualization (rather than slow performance data analysis with suboptimal charts, graphs or histograms hindering easy and correct data interpretation). The MITOMATICS wet-plus-dry pipeline has been specifically designed for high-throughput phenotyping of mitochondrial morphology by miniaturizing and automating high-resolution

imaging before an in-house software application (MitoRadar) handles all fundamental operations from image segmentation to statistical analysis and drawing meaningful interpretation from custom mito-signatures (Fig. 1). The use of 96-well plates with random imaging of 5 fields per well enables analysis of multiple experimental conditions while achieving robust results. To image mitochondria in their cellular context, we use the potentiometric dye MitoTracker Deep Red (MTDR) in combination with fluorescent markers (green and blue, respectively) specific for cellular membranes (Cell Mask Green) and nuclei (Hoechst 33342). Confocal images are acquired on an Opera Phenix® High-Content Screening (HCS) System (equipped in its optimal configuration with a robotic arm and incubator) and directly loaded into the MitoRadar software to perform the post-acquisition steps. This software uses deep learning during the image segmentation phase (Fig. S1) and calculates about a hundred morphological descriptors (Table S1), offering one of the most comprehensive sets of parameters to infer mitochondrial (network) shape and overall cell morphology. The MitoRadar software enables the detection and assessment of subtle morphological characteristics, undetectable or barely detectable through conventional methods and has advanced analytical, statistical and graphical features for data representation, analysis and interpretation. Our miniaturized technology suits diverse applications among which are: testing the noxious effect of individual molecules on the mitochondrial network (*MitoCollapse* module for predictive toxicology) ; testing the deleterious effects of combinations of molecules, drugs or pollutants (*MitoCocktail* module for predictive as well as environmental toxicology) ; assessing changes in mitochondrial morphology in pathological (or aged) cells compared to their non-pathological (or 'young') counterparts (*MitoMedCare* module) and objectifying the beneficial effects of cosmetic or pharmacological bioactive ingredients (*MitOasis* module) (Fig. 1). In the present report, we focus only on the first two applications.

3.1.2.Implementation of the MitoRadar software

Here, we sought to validate our fully automated image analysis pipeline on rich datasets gathered from cultured live human cells exposed to specific chemicals known to induce either mitochondrial fragmentation (CCCP, Rot, Ant A) (29–32) or mitochondrial hyperfusion (MDIVI-1, M1) (33,34).

Eight human cell lines of normal and diseased states, from different tissue origin, were successfully imaged (Fig. S2), leading to an image database of approximately 30,000 microphotographs (named 'MITOPIX-DEV', DEV standing for 'development') that was used to develop the MitoRadar software. Representative images are shown in Fig. 2 for BEAS-2B cells (see Fig. S3 for the other cell lines), a human lung epithelial cell line that has been widely used in toxicity tests, specifically to assess the deleterious effects of heavy metals (35), microplastics (36), fine particles (37) and pesticides (38).

Based on MITOPIX-DEV, the MitoRadar software was implemented, optimized and extensively debugged over a six-month period. Several functionalities were implemented: (i) an AI image segmentation module (using deep learning) to detect cells, nuclei and mitochondria (Fig 3A, 3B panel a and Fig. S1 A); (ii) a quantification module to characterize the detected objects with advanced descriptors (n=104, see Table S1 for the exhaustive list); note that for each descriptor, 4 distribution aggregators were computed: mean, variance, skewness and kurtosis, allowing for a more refined and realistic description of the objects under study; (iii) a database with its dedicated interface dynamically linking the data and metadata of the experiments (Fig. 3B panel b); and finally (iv) an interface for integrated analysis (including statistics) and easy visualization of the results (Fig. 3B panels c-d and Fig. 3C).

MitoRadar provides a comprehensive analysis of the morphological characteristics of the mitochondriome of cells by performing morphometric measurements at the supra-mitochondrial, mitochondrial and sub-mitochondrial levels. The computer program is multiscalar, allowing to navigate over a diverse range of scales (isolated mitochondria, clusters of mitochondria, subcellular locations, cells, cell cultures) (Fig. S1B) and multidimensional, multivariate quantitative data being readily visualizable through innovative radar charts. Each variable is represented along the X-axis. The computed parameters are compared to a reference situation (blue circle) and parameters showing statistically significant deviation are displayed along a heat map Y-axis (the size of the points along the curve reflecting the degree of statistical significance). Six different MitoRadar plots can be created by grouping the parameters associated with single or networked mitochondria, the total mitochondrial complement present in a given cell (mitochondriome), cellular features, nuclear features and attributes

of the *counter shape* (i.e., inverted selection of the cellular region containing labelled mitochondria, to our best knowledge this latter category of descriptors being completely new in the field) (see Fig. 3C). Parameters that show little or no variation compared to the control are listed in brown, those that decrease or increase are respectively colored in blue and red, with fixed rank ordering or (according to user preference) with a rank assigned in descending or ascending order.

Results are generated in the form of reports of decreasing complexity, integrating statistical analysis and advanced graphical representation tools (two functionalities absent from most image analysis software, which require separate manual processing by a trained operator). The colors and their intensities are correlated with the size of the measured effects, and statistical significance is represented by circles of increasing diameter (Fig. 3C). The user can choose between PCA, LDA, correlation map or dendrogram, T-Test with corrections for multiple comparisons, and SSMD (Fig. 3B panels c-d). All of these advanced statistical tests are natively integrated into MitoRadar's user-friendly graphical interface, which makes them accessible without any third-party software to biologists who do not have programming skills. It also makes it easy to share projects, images, and quantifications.

3.1.3. MitoRadar validation on high-throughput microscopy images of cells treated with the mitochondrial uncoupler CCCP

During cellular stress when ROS accumulates the mitochondrial network becomes largely fragmented (39). CCCP, an inhibitor of mitochondrial oxidative phosphorylation, evokes the integrated stress response and its application to cells results in dramatic fragmentation of mitochondria (29,30). To test the performance of MitoRadar as a big data analytics software, we treated BEAS-2B cells with 20µM CCCP during 4h (Fig. 4A). Five independent experiments were done with more than 200,000 cells analyzed, representing about 32,580 microphotographs and a total processing time of around 260 minutes (for the whole project). The three upper MitoRadar plots of Fig. 4B show a massive and highly significant variation of more than 90% of the descriptors (55/61) related to the mitochondrial phenotype, most of them (47) with $p<0.001$*** (Mann Whitney Test with Benjamini Hochberg correction). Among

the descriptors that decrease (in blue) and account for size reduction of both mitochondria and mitochondrial (sub)networks, we find area_mean, aspect_ratio_mean, axis_major_length_mean and axis_minor_length_mean, equivalent_diameter_area_mean, feret_diameter_max_mean and perimeter_crofton_mean.

Mitochondrial fragmentation is evidenced by the augmentation (in red) of circularity and roundness. Smaller degrees of mitochondrial interconnection and branching are evidenced by the decrease in skeleton length and number of branch points (skel_length_mean, branch_points_mean, clusterised_mito and clustering_coef). Consistent with this dislocation of the mitochondrial reticulum, the number of mitochondria and specifically of isolated mitochondria appears greater. Texture as well as density profiles undergo concomitant variations as indicated by increase in solidity_mean and in Euler number means, which relate to the number of holes in the analyzed cells when mitochondria and mitochondrial clusters are considered (Fig. 4B, top right panels) and in their inferred negative shapes or *countershape* (Fig. 4B, bottom middle panel). Subcellular distribution of the mitochondria also reflects cellular stress as shown by their positioning away from the cell membrane and closer to the nucleus.

Compared to mitochondrial parameters, changes in cellular parameters are less drastic (Fig. 4B, bottom right plot) and suggest slight spreading of the cells. Because the set of nuclear parameters (n=18) does not display any significant change at all (Fig. 4B, bottom left plot), our data demonstrate that MitoRadar objectively measures mitochondria-damaging effects before the onset of early apoptotic features (such as the appearance of highly condensed pyknotic nuclei, cell shrinking and blebbing). These mitochondria-damaging effects are described as 'large' by an in-house scoring system, MitoScore (Fig. 4C), which comprises a color-coded scale and a summary of the most affected parameters (see *Methods* for details).

MitoRadar software natively offers a range of both basic and fairly advanced statistical tools for data analysis, such as PCA, LDA and violin plots (i.e., hybrids of box plots and kernel density plots) (Fig. 4D). Details on SSMD values (Fig. S4 A), u-values (Fig. S4 B) and p-values (Fig. S4 C) were also plotted separately for better clarity (readability) and counting of u-values. Lastly, note that

mitochondrial descriptors show a high level of correlation on both correlation dendrogram (or hierarchical clustering diagram) (Fig. S4 D) and distance map (Fig. S4 E), revealing a global transformation of the mitochondrial component. The PCA plot shows that the control and CCCP conditions clearly segregate into two distinct groups (Fig. 4D, panel a). Projection of the descriptors onto the axes of the PCA confirms that the observed variations are mainly due to changes in mitochondrial features (Fig. S4 F). LDA with prior knowledge of class labels improves the observed segregation between the control and CCCP-treated groups (Fig. 4D, panel b and Fig. S4 G). Violin plots are useful for plotting variations in individual descriptors as exemplified here by the Mito roundness_mean variable (Fig. 4D, panel c). Altogether, our results suggest that MitoRadar operates quickly, efficiently, reliably and cost-effectively to distinguish a highly fragmented mitochondrial network from a normal, healthy one using live-cell fluorescence microscopy images of cultured mammalian cells.

3.1.4.MitoCollapse: assessing acute mitochondrio-toxicity of single pesticides in vitro

Exposure to anthropogenic pollutants is a critical biomedical and ecological issue, pesticides being potentially hazardous to human health and one of the main contributors to environmental deterioration. We hypothesized that our approach could be useful to assess the in vitro mitochondrial toxicity of a selection of pesticides, taking CCCP as an internal positive control of cell poisoning. Four different fungicides were chosen, including the two ETC complex II inhibitors Mepronil (MEP) and Thifluzamide (THI) as well as Azoxystrobin (AZO) and Pyraclostrobin (PYRA), which are two ETC complex III inhibitors, plus the two acaricides Fenpyroximate (FEN) and Pyridaben (PYRI), which are ETC complex I inhibitors.

Pulmonary BEAS-2B cells were treated with various concentrations (10, 50, 100, 250 and 500 µM) of individual pesticides and images were taken 2h after pesticide exposure. The threshold dose (i.e., the dose below which MitoRadar plots show no variation compared to control) and LD50 (i.e, the dose for which 50% of cells died 24h after) were then evaluated (Fig 5A). MitoRadar analysis corresponding to

features obtained with the 250µM dose (Fig. 5B) showed a clear disruption of mitochondria and their networks in cells following single pesticide treatment, compared to control cells, resulting into a MitoScore transitioning from '*Substantial overall effect*' to '*Large overall effect*' (Fig. 5C).

Like CCCP, all of these pesticides appeared to trigger mitochondrial fragmentation when applied at a dose of 250µM, MitoRadar plots showing an increase in the circularity_mean, roundness_mean, and isolated_mito parameters with concomitant decrease in skel_length_mean, area_mean, axis_major_length_mean and axis_minor_length_mean.

Interestingly, analysis with MitoRadar also revealed several unexpected differences between the measured effects of the various pesticides. For example, average length of the minor axis of mitochondria decreased after treatment with CCCP, THI and PYRA, while a significant increase was observed for this parameter with the other pesticides. Likewise, the number of mitochondria was increased for CCCP as well MET and THI (inhibitors of complex II) and decreased for AZO and PYRA (inhibitors of complex III). When LDA was carried out on defined pairs of pesticides according to their type of ETC inhibition, untreated controls were well separated from the defined groups (as well as from the CCCP-treated group) by the first two discriminant axis (Fig. 5D).

Compared to the negative control (vehicle), the Mito euler_number_mean, which reflects the number of holes in the mitochondrial network, was smaller for the group of Complex III inhibitors, followed by Complex II and I inhibitors, while skeleton length values progressively decreased with ETC inhibitors I, III and II.

Nuclear parameters related to size tended to increase for CCCP while they decreased significantly for PYRA. Few variations of the cell and countershape features were detected as shown on the MitoRadar plots (Fig. S5 A). Details of the statistical analyses are presented in Fig. S5 (correlation distance MAP Fig. S5 B; SSMD summary Fig. S5 C; U-Value Fig. S5 D).

Therefore, although as a first approximation the mitochondrial response to the tested single toxicants was assumed to be similar (with pesticide treatment resulting in mitochondrial fragmentation), using

built-in statistical analysis modules, MitoRadar analysis was able to reveal subtle changes in the deep architecture of mitochondrial structures.

3.1.5.MitoCocktail: assessing acute mitochondrio-toxicity of pesticide mixtures in vitro

We took advantage of MITOMATICS for assessing the mitochondrial toxicity of pesticides administered in combination on cultured BEAS-2B cells, according to real-world data (40) produced by ATMO-Occitanie, the accredited association for air quality monitoring in the Occitanie Region (France). Annual campaigns to measure pesticides in the ambient air have been carried out over 12 months since 2014 in a rural environment dominated by wine, arboriculture or field crops. Based on the cumulative concentrations of the fifteen most commonly found pesticide residues in the different departments of Occitanie (Tarn-et-Garonne, Pyrénées-Orientales, Lauragais, Aude and Gard), the top five air-borne pesticides were selected for further analysis. The list of pesticides under study comprised two fungicides, Folpel (FOL) and Cyprodinil (CYP), one herbicide, Pendimethaline (PEN) and two insecticides, Lindane (LIN, banned since 1998) and Chlorpyriphos methyl (CHL) (Fig. 6A).

First, these five pesticides were tested separately (as above) on BEAS-2B cells for 4h at various concentrations ranging from 10 to 500 µM to determine the threshold dose. After 24h, the number of cells was recorded in each condition and the LD50 was calculated. A summary of the results from 4 independent experiments (representing about 100,000 analyzed cells) is presented in Fig. 6A.

Next, to determine if the pesticides can be more noxious when combined (a phenomenon known as the 'cocktail effect'), we prepared mixtures with relative proportions of pesticides based on the ATMO report. Note that the identity of the most prominent pesticide (which was tested at concentrations ranging from 10 to 500µM) varied across departments, representing between 78% and 97% of the final mixture (Fig. 6B).

Our data indicate that both the threshold dose and the acute LD50 of pesticide mixtures were at least five times lower than that of individual pesticides in all considered departments (Fig. 6A and B). The case of Aude is taken here as an illustration. In this department, FOL is the main air-borne pesticide

(97%), whereas the three other pesticides (PEN, CHL and LIN) are present as traces (in the following proportions: 1.1%, 0.8% and 1.5%, respectively).

Mitochondrial disorganization was observable microscopically (Fig. 6C) and measurable through MitoRadar analysis (Fig. 6D) when 10µM FOL was mixed with low concentrations of the other pesticides (0.11µM PEN; 0.15µM CHL and 0.08µM LIN), i.e., when each individual pesticide was present at levels below its "no-observed-effect-concentration" (threshold doses were 50µM for FOL; >500µM for PEN; 100µM for CHL and 500µM for LIN).

The computed MitoScore (based on the top 15 most affected parameters) indicated weak to moderate effects when cells were exposed to single pesticides at a 10µM concentration and maximal noxious effect with the pesticide mixture (Fig. 6E). In conclusion, traces of PEN, CHL and LIN potentiate both the mitochondrial and cellular toxicity of FOL. Note that similar conclusions can be drawn for the pesticide combinations characteristic of the other four departments.

4. Discussion

Mitochondria are membrane-enclosed organelles ubiquitously found in eukaryotes. Originally derived from endosymbiotic bacteria, they play a vital role in energy production and in many other cellular functions (2,41). It is considered that all physicochemical, parasitic and microbial influences that surround eukaryotic life are translated into changes in mitochondrial structure and function (42–47). In particular, a growing body of literature points to mitochondria as a key organelle targeted by environmental pollutants (3–5,48–53). Not only do these environmental pollutants (present in air, water and soil) disturb the mitochondrial machinery but their mitotoxicity may cause significant damage to the epigenome and transgenerational inheritance of dysfunctional mitochondria (4). Mitochondria are thus considered to provide the missing link between cellular, organismal and environmental health (10).

As 'mitochondrial form follows function' (54), previous studies highlighted the utility of using mitochondrial morphology as a proxy for monitoring cell health and cytotoxicity (17,46,55–59). In this paper, we described a comprehensive and user-friendly big data analytics software (MitoRadar)

combined with a HCS wet pipeline (MITOMATICS) to analyze mitochondrial shape changes occurring in live cultured cells. We applied our image-based phenotypic profiling system to assess mitochondrial architecture in response to environmental pollutants. This system was designed to replace traditional, costly and low-throughput techniques, which will be reserved for downstream validation on prioritized combinations.

Because mitochondrial changes appear to happen before other cellular events, shorter incubation durations are needed, this approach thus saves time and money while enhancing efficiency. While most available tools require programming experience or computer science skills, the core component of our workflow involves an easy-to-work-with and intuitive in-house, proprietary software (MitoRadar). Live-cell, high-resolution confocal images are collected on any multiplexed imaging platforms available and from any type of cells cultured on 96-well plates and stained with different vital dyes (with one of them labelling mitochondria), before processing of a large number of images at various possible scales, AI-driven segmentation and automatic calculation by MitoRadar of 2D descriptors associated with the identified mitochondria in their cellular context.

By quickly computing more than one hundred descriptors related to mitochondria (some of which being novel like the '*Countershape'*) and additional nuclear and cellular shape parameters, MitoRadar represents one of the most comprehensive software packages available for image analysis. Our automated and miniaturized approach integrates a convenient way for interpreting the gathered massive and multidimensional data by creating unique radar plots in which sample datasets (e.g. from cells treated with chemicals) are compared to a reference dataset (i.e., untreated or mock-treated cells). These information-rich representations natively come up with a variety of statistical charts and plots (t-tests, PCA, LDA, violin distributions) and with a simple score (MitoScore), making it quick and easy to compare the impact of various substances or culture conditions and to detect subtle morpho-phenotypic variations. It is remarkable that our method was able to discriminate the effect of molecules acting at different stages of mitochondrial function, namely CCCP (a widely used mitochondrial uncoupler), Rotenone (Complex I inhibitor) and Antimycin (Complex III inhibitor). Besides CCCP and other traditional uncouplers (like FCCP or 2,4-dinitrophenol), novel mitochondria-specific uncoupling agents

such as BAM15 and FR58P1 (60) or the organic pollutant pentachlorophenol (61) were identified that could be tested using our technology to improve our knowledge of the consequences of mitochondrial uncoupling on mitochondrial network architecture. In addition to Antimycin A, which is specific to the N-side quinone binding site of Complex III, it would be interesting to assess the effects of Myxothiazol, which acts at the P-side. Inhibitors of Complex IV (potassium cyanide, sodium azide or lipophilic small molecules like steroids) and ATP synthase inhibitors like oligomycin and dicyclohexylcarbodiimide (DCCD), which respectively bind to the F_O and F_OF_1 subunits of the proton pump, are also worth testing.

Here, we applied our technology to test the noxious potential of single pollutants (*MitoCollapse*) as well as combination effects between molecules (*MitoCocktail*).

Regarding *MitoCollapse*, we recently collected results on single exposure of skin cells to three pesticides (two insecticides, fipronil and imidacloprid as well as glyphosate, present in the widely used herbicide Roundup®) (Charrasse et al. submitted) and, in the present study, of non-tumorigenic lung cells to eleven additional pesticides including five currently detected in Occitanie (Southern France). This research is in line with classic toxicology studies carried out by various organizations such as the National Institute of Environmental Health Sciences through its National Toxicology Program (NTP). Interestingly, the mitochondrial 'morpho-signatures' of the six chemicals that we tested so far as individual substances appear not only to be distinct but also to segregate into discrete families, suggesting that the effects of pesticides (and virtually of any environmental pollutant(s)) might be classified within a 'morphospace' of mitochondriome morphologies. It would be interesting to determine whether specific signatures are linked to particular physicochemical properties of pesticides or to their toxicological profile.

The combined effects of chemical mixtures, a rapidly emerging topic in environmental toxicology (62), prompted us to design another module, *MitoCocktail*, for estimating the mitochondrial response of a larger number of substances, across a battery of concentrations and in combination. This functionality currently handles projects using a single dose response of combined drugs, rather than a full two-way matrix of varying doses, similar to other HCS studies. Mixture effects are usually classified as being antagonistic, additive or synergistic, depending on whether the observed toxicity of the combination is

lower than, equal to, or higher than the expected toxicity based on an additivity model. Thanks to pollutant data made available by ATMO-Occitanie, we showed that the deleterious effects on mitochondrial architecture and cellular viability of the main pesticide found in each department of Occitanie were enhanced when trace quantities of other pesticides were added, indicative of synergistic relationships.

MitoRadar analysis can help decipher human health impacts of anthropogenic chemicals found in the air, but also in water, food and soil. In addition to pesticides, various sources of pollution can be studied, such as fine particles, polycyclic aromatic hydrocarbons, plastics, pharmaceutical waste, cosmetics and even antibiotics (63) or noise pollution (64). Samples taken from natural environments and containing unidentified pollutants or metabolites may also be blind tested. Beyond exposure to pollutants, other variables may be considered such as genetic or epigenetic contexts, age, disease, diet and physical exercise that are likely to influence mitochondrial health. Our method is also suitable for analyzing primary cells from different organs or tissues of patients with particular life histories, such as for instance type 2 diabetes (65) or autism spectrum disorder (66), in order to gain better understanding of the mitochondrial correlates of pathophysiology. In that respect, it would be of interest to assay the morphometric parameters of mitochondria in cell lines derived from children with autistic disorder (in comparison to paired cells lines from typically developing siblings or control cell lines) with or without exposure to environmental factors such as air pollution or pesticides (67–70). This is indeed very relevant to this population as studies have shown changes in mitochondrial respiration with exposure to toxicants such as air pollution (69) and other common toxicants (71) in children with autism. This technique could be applied to disease populations to understand how environmental agents may produce disease through effects on bioenergetics. Taking up the One Health perspective (72,73), non-mammalian cell lines may also be tested including honeybee or zebrafish cell lines. Indeed, several pesticides (e.g. succinate dehydrogenase inhibitors, SDHIs) that are toxic to mitochondria act by blocking cellular respiration. This property, used to eliminate certain fungi, mites or worms, makes them potentially toxic for all living beings.

The MITOMATICS technology can be combined with phenotypic/functional analysis (e.g. measurement of mitochondrial activities through ELISA plate readers and spectrophotometric methods, determination of apoptosis/necrosis rates by flow cytometry) and followed by more specialized readouts including measuring oxygen consumption and extracellular acidification rates (using Seahorse®), mitochondrial iron content through biochemical techniques or the uptake of specific fluorescent probes (like DCFH-DA for detecting ROS) by flow cytometry or fluorescent imaging. For example, in a recent study (66), mitochondrial morphology paralleled variations in respiratory rates in fibroblasts derived from patients and healthy controls, thereby allowing the validation of the respiratory changes and a better understanding of the consequence of these changes in mitochondrial respiration.

Our approach may be improved in a number of ways. In particular, the mitochondriome should be viewed as a four-dimensional architecture (X,Y,Z + time) whose configuration may evolve due to mitochondrial fission, fusion and motility as well as cell movements (including various extension of the cell surface, migration and division). Albeit non-amenable to HCS screening, future MITOMATICS developments will use bioimaging techniques that could capture mitochondria in 4D, such as lattice light-sheet microscopy (LLSM) and three-dimensional structured illumination microscopy (3D SIM). For now, our method for 2D automated quantification of mitochondrial morphology appears to be well-suited for relatively 'flat' cells, i.e., cells where mitochondria are confined to a limited number of planes. Utilization of cells cultured in 3D (through different systems including spheroids, hydrogels or scaffolds) could improve physiological relevance for certain cell types (like endothelial cells or mixed cell populations such as in 3D reconstituted skin) or conditions (e.g. growth of cancer cells).

5. Conclusions

In vitro assessment of mitochondrial toxicity through our novel quantitative imaging system can be useful to draft prioritized lists of deleterious chemicals, ranked according to their impact on mitochondria, before functional tests and in vivo assays are conducted. Our HCS system may also serve as a valuable tool to transition from the current single-chemical-based risk paradigm towards one which addresses co-exposures to multiple chemicals, and more generally to multiple stressors due to external exposome and/or pathological conditions.

6. Acknowledgements

We thank Mylène Weill, Nicolas Galtier, Sébastien Gibert, Sébastien Picard and Florence Saïdani at ISEM for their support. The authors are grateful to Florence Grange (INEE), Patricia Verwaerde (DR13 CNRS), Sylvain Lamare, Benjamin Morlon and Jean-Marc Schmittbiel at CNRS Innovation. We acknowledge the imaging facility MRI, member of the France-BioImaging national infrastructure supported by the French National Research Agency (ANR-10-INBS-04, "Investments for the future"). Special thanks go to Elodie Jublanc, Vicky Diakou, and Cédric Hassen-Khodja for expert assistance with confocal microscopy, experimental design and statistics, to the Montpellier Meditérannée Métropole Business & Innovation Center (BIC) staff and to Brigitte Couette, Julia Van Bockstaele and Ava Halloran for help and fruitful discussions.

7. Funding statement

This work was supported by grants from the i-site MUSE (KIM "Biomarkers and Therapy"), Ligue contre le Cancer - Comité du Gard (n° 176487), Fondation ARC pour la recherche sur le cancer (n° 172351) and CNRS Prematuration program MITOMATIQUE (04/2021).

8. References

1. Nunnari J, Suomalainen A. Mitochondria: in sickness and in health. Cell. 2012 Mar 16;148(6):1145–59.
2. Monzel AS, Enríquez JA, Picard M. Multifaceted mitochondria: moving mitochondrial science beyond function and dysfunction. Nat Metab. 2023 Apr;5(4):546–62.
3. Meyer JN, Hartman JH, Mello DF. Mitochondrial Toxicity. Toxicol Sci. 2018 Mar 1;162(1):15–23.

4. Duarte-Hospital C, Tête A, Brial F, Benoit L, Koual M, Tomkiewicz C, et al. Mitochondrial Dysfunction as a Hallmark of Environmental Injury. Cells. 2021 Dec 30;11(1):110.

5. Reddam A, McLarnan S, Kupsco A. Environmental Chemical Exposures and Mitochondrial Dysfunction: a Review of Recent Literature. Curr Environ Health Rep. 2022 Dec;9(4):631–49.

6. Luo Y, Ma J, Lu W. The Significance of Mitochondrial Dysfunction in Cancer. Int J Mol Sci. 2020 Aug 5;21(16):5598.

7. Frye RE, Lionnard L, Singh I, Karim MA, Chajra H, Frechet M, et al. Mitochondrial morphology is associated with respiratory chain uncoupling in autism spectrum disorder. Transl Psychiatry. 2021 Oct 13;11(1):527.

8. Bornstein R, Gonzalez B, Johnson SC. Mitochondrial pathways in human health and aging. Mitochondrion. 2020 Sep;54:72–84.

9. Aouacheria A, Baghdiguian S, Lamb HM, Huska JD, Pineda FJ, Hardwick JM. Connecting mitochondrial dynamics and life-or-death events via Bcl-2 family proteins. Neurochem Int. 2017 Oct;109:141–61.

10. Naviaux RK. Perspective: Cell danger response Biology-The new science that connects environmental health with mitochondria and the rising tide of chronic illness. Mitochondrion. 2020 Mar;51:40–5.

11. Friedman JR, Nunnari J. Mitochondrial form and function. Nature. 2014 Jan 16;505(7483):335–43.

12. Sprenger HG, Langer T. The Good and the Bad of Mitochondrial Breakups. Trends Cell Biol. 2019 Nov;29(11):888–900.

13. Leonard AP, Cameron RB, Speiser JL, Wolf BJ, Peterson YK, Schnellmann RG, et al. Quantitative analysis of mitochondrial morphology and membrane potential in living cells using high-content imaging, machine learning, and morphological binning. Biochim Biophys Acta. 2015 Feb;1853(2):348–60.

14. Peng JY, Lin CC, Chen YJ, Kao LS, Liu YC, Chou CC, et al. Automatic morphological subtyping reveals new roles of caspases in mitochondrial dynamics. PLoS Comput Biol. 2011 Oct;7(10):e1002212.

15. Reis Y, Bernardo-Faura M, Richter D, Wolf T, Brors B, Hamacher-Brady A, et al. Multi-parametric analysis and modeling of relationships between mitochondrial morphology and apoptosis. PLoS One. 2012;7(1):e28694.

16. Harwig MC, Viana MP, Egner JM, Harwig JJ, Widlansky ME, Rafelski SM, et al. Methods for imaging mammalian mitochondrial morphology: A prospective on MitoGraph. Anal Biochem. 2018 Jul 1;552:81–99.

17. Zahedi A, On V, Phandthong R, Chaili A, Remark G, Bhanu B, et al. Deep Analysis of Mitochondria and Cell Health Using Machine Learning. Sci Rep. 2018 Nov 5;8(1):16354.

18. Rohani A, Kashatus JA, Sessions DT, Sharmin S, Kashatus DF. Mito Hacker: a set of tools to enable high-throughput analysis of mitochondrial network morphology. Sci Rep. 2020 Nov 3;10(1):18941.

19. Ahmad T, Aggarwal K, Pattnaik B, Mukherjee S, Sethi T, Tiwari BK, et al. Computational classification of mitochondrial shapes reflects stress and redox state. Cell Death Dis. 2013 Jan 17;4(1):e461.

20. Hemmerich J, Troger F, Füzi B, F Ecker G. Using Machine Learning Methods and Structural Alerts for Prediction of Mitochondrial Toxicity. Mol Inform. 2020 May;39(5):e2000005.

21. Giedt RJ, Fumene Feruglio P, Pathania D, Yang KS, Kilcoyne A, Vinegoni C, et al. Computational imaging reveals mitochondrial morphology as a biomarker of cancer phenotype and drug response. Sci Rep. 2016 Sep 9;6:32985.

22. Jugé R, Breugnot J, Da Silva C, Bordes S, Closs B, Aouacheria A. Quantification and Characterization of UVB-Induced Mitochondrial Fragmentation in Normal Primary Human Keratinocytes. Sci Rep. 2016 Oct 12;6:35065.

23. Stringer C, Wang T, Michaelos M, Pachitariu M. Cellpose: a generalist algorithm for cellular segmentation. Nat Methods. 2021 Jan;18(1):100–6.

24. Ronneberger O, Fischer P, Brox T. U-Net: Convolutional Networks for Biomedical Image Segmentation. In: Navab N, Hornegger J, Wells WM, Frangi AF, editors. Medical Image Computing and Computer-Assisted Intervention – MICCAI 2015 [Internet]. Cham: Springer International Publishing; 2015 [cited 2023 Sep 16]. p. 234–41. (Lecture Notes in Computer Science; vol. 9351). Available from: http://link.springer.com/10.1007/978-3-319-24574-4_28

25. Kromp F, Fischer L, Bozsaky E, Ambros IM, Dorr W, Beiske K, et al. Evaluation of Deep Learning Architectures for Complex Immunofluorescence Nuclear Image Segmentation. IEEE Trans Med Imaging. 2021 Jul;40(7):1934–49.

26. Waisman A, Norris AM, Elías Costa M, Kopinke D. Automatic and unbiased segmentation and quantification of myofibers in skeletal muscle. Sci Rep. 2021 Jun 3;11(1):11793.

27. Pachitariu M, Stringer C. Cellpose 2.0: how to train your own model. Nat Methods. 2022 Dec;19(12):1634–41.

28. Zhang TY, Suen CY. A fast parallel algorithm for thinning digital patterns. Commun ACM. 1984 Mar;27(3):236–9.

29. Ishihara N, Jofuku A, Eura Y, Mihara K. Regulation of mitochondrial morphology by membrane potential, and DRP1-dependent division and FZO1-dependent fusion reaction in mammalian cells. Biochem Biophys Res Commun. 2003 Feb 21;301(4):891–8.

30. Miyazono Y, Hirashima S, Ishihara N, Kusukawa J, Nakamura KI, Ohta K. Uncoupled mitochondria quickly shorten along their long axis to form indented spheroids, instead of rings, in a fission-independent manner. Sci Rep. 2018 Jan 10;8(1):350.

31. Leonard AP, Cameron RB, Speiser JL, Wolf BJ, Peterson YK, Schnellmann RG, et al. Quantitative analysis of mitochondrial morphology and membrane potential in living cells using high-content imaging, machine learning, and morphological binning. Biochim Biophys Acta. 2015 Feb;1853(2):348–60.

32. Tauber J, Dlasková A, Šantorová J, Smolková K, Alán L, Špaček T, et al. Distribution of mitochondrial nucleoids upon mitochondrial network fragmentation and network reintegration in HEPG2 cells. Int J Biochem Cell Biol. 2013 Mar;45(3):593–603.

33. Maneechote C, Chattipakorn SC, Chattipakorn N. Recent Advances in Mitochondrial Fission/Fusion-Targeted Therapy in Doxorubicin-Induced Cardiotoxicity. Pharmaceutics. 2023 Apr 7;15(4):1182.

34. Maneechote C, Chattipakorn SC, Chattipakorn N. Recent Advances in Mitochondrial Fission/Fusion-Targeted Therapy in Doxorubicin-Induced Cardiotoxicity. Pharmaceutics. 2023 Apr 7;15(4):1182.

35. Cao X, Fu M, Bi R, Zheng X, Fu B, Tian S, et al. Cadmium induced BEAS-2B cells apoptosis and mitochondria damage via MAPK signaling pathway. Chemosphere. 2021 Jan;263:128346.

36. Dong CD, Chen CW, Chen YC, Chen HH, Lee JS, Lin CH. Polystyrene microplastic particles: In vitro pulmonary toxicity assessment. J Hazard Mater. 2020 Mar 5;385:121575.

37. Sotty J, Kluza J, De Sousa C, Tardivel M, Anthérieu S, Alleman LY, et al. Mitochondrial alterations triggered by repeated exposure to fine (PM2.5-0.18) and quasi-ultrafine (PM0.18) fractions of ambient particulate matter. Environ Int. 2020 Sep;142:105830.

38. Kanno S, Hirano S, Mukai T, Ro A, Kato H, Fukuta M, et al. Cellular uptake of paraquat determines subsequent toxicity including mitochondrial damage in lung epithelial cells. Leg Med (Tokyo). 2019 Mar;37:7–14.

39. Perdiz D, Oziol L, Poüs C. Early mitochondrial fragmentation is a potential in vitro biomarker of environmental stress. Chemosphere. 2019 May;223:577–87.

40. Langevine A. La lettre de l'Air n°19 [Internet]. Atmo Occitanie, observatoire régional de l'air; 2022. Available from: https://www.atmo-occitanie.org/sites/default/files/publications/2022-03/Lettre%20de%20l%27air%20n%C2%B019%20La%20surveillance%20des%20pesticides%20dans%20l%27air%20en%202019-20.pdf

41. Roger AJ, Muñoz-Gómez SA, Kamikawa R. The Origin and Diversification of Mitochondria. Curr Biol. 2017 Nov 6;27(21):R1177–92.

42. Wan X, Garg NJ. Sirtuin Control of Mitochondrial Dysfunction, Oxidative Stress, and Inflammation in Chagas Disease Models. Front Cell Infect Microbiol. 2021;11:693051.

43. Wang Y, Li N, Zhang X, Horng T. Mitochondrial metabolism regulates macrophage biology. J Biol Chem. 2021 Jul;297(1):100904.

44. Nunnari J, Suomalainen A. Mitochondria: in sickness and in health. Cell. 2012 Mar 16;148(6):1145–59.

45. Bornstein R, Gonzalez B, Johnson SC. Mitochondrial pathways in human health and aging. Mitochondrion. 2020 Sep;54:72–84.

46. Aouacheria A, Baghdiguian S, Lamb HM, Huska JD, Pineda FJ, Hardwick JM. Connecting mitochondrial dynamics and life-or-death events via Bcl-2 family proteins. Neurochem Int. 2017 Oct;109:141–61.

47. Friedman JR, Nunnari J. Mitochondrial form and function. Nature. 2014 Jan 16;505(7483):335–43.

48. Strilbyska OM, Tsiumpala SA, Kozachyshyn II, Strutynska T, Burdyliuk N, Lushchak VI, et al. The effects of low-toxic herbicide Roundup and glyphosate on mitochondria. EXCLI J. 2022;21:183–96.

49. Ferramosca A, Lorenzetti S, Di Giacomo M, Murrieri F, Coppola L, Zara V. Herbicides glyphosate and glufosinate ammonium negatively affect human sperm mitochondria respiration efficiency. Reprod Toxicol. 2021 Jan;99:48–55.

50. Pereira SP, Santos SMA, Fernandes MAS, Deus CM, Martins JD, Pedroso de Lima MC, et al. Improving pollutants environmental risk assessment using a multi model toxicity determination with in vitro, bacterial, animal and plant model systems: The case of the herbicide alachlor. Environ Pollut. 2021 Oct 1;286:117239.

51. Peters A, Nawrot TS, Baccarelli AA. Hallmarks of environmental insults. Cell. 2021 Mar 18;184(6):1455–68.

52. Lim S, Ahn SY, Song IC, Chung MH, Jang HC, Park KS, et al. Chronic exposure to the herbicide, atrazine, causes mitochondrial dysfunction and insulin resistance. PLoS One. 2009;4(4):e5186.

53. Xu S, Pi H, Chen Y, Zhang N, Guo P, Lu Y, et al. Cadmium induced Drp1-dependent mitochondrial fragmentation by disturbing calcium homeostasis in its hepatotoxicity. Cell Death Dis. 2013 Mar 14;4(3):e540.

54. Wang C, Youle R. Cell biology: Form follows function for mitochondria. Nature. 2016 Feb 18;530(7590):288–9.

55. Lihavainen E, Mäkelä J, Spelbrink JN, Ribeiro AS. Mytoe: automatic analysis of mitochondrial dynamics. Bioinformatics. 2012 Apr 1;28(7):1050–1.

56. Peng JY, Lin CC, Chen YJ, Kao LS, Liu YC, Chou CC, et al. Automatic morphological subtyping reveals new roles of caspases in mitochondrial dynamics. PLoS Comput Biol. 2011 Oct;7(10):e1002212.

57. Ahmad T, Aggarwal K, Pattnaik B, Mukherjee S, Sethi T, Tiwari BK, et al. Computational classification of mitochondrial shapes reflects stress and redox state. Cell Death Dis. 2013 Jan 17;4(1):e461.

58. Vowinckel J, Hartl J, Butler R, Ralser M. MitoLoc: A method for the simultaneous quantification of mitochondrial network morphology and membrane potential in single cells. Mitochondrion. 2015 Sep;24:77–86.

59. Valente AJ, Maddalena LA, Robb EL, Moradi F, Stuart JA. A simple ImageJ macro tool for analyzing mitochondrial network morphology in mammalian cell culture. Acta Histochem. 2017 Apr;119(3):315–26.

60. Demine S, Renard P, Arnould T. Mitochondrial Uncoupling: A Key Controller of Biological Processes in Physiology and Diseases. Cells. 2019 Jul 30;8(8):795.

61. Xia M, Huang R, Shi Q, Boyd WA, Zhao J, Sun N, et al. Comprehensive Analyses and Prioritization of Tox21 10K Chemicals Affecting Mitochondrial Function by in-Depth Mechanistic Studies. Environ Health Perspect. 2018 Jul;126(7):077010.

62. Rietdijk J, Aggarwal T, Georgieva P, Lapins M, Carreras-Puigvert J, Spjuth O. Morphological profiling of environmental chemicals enables efficient and untargeted exploration of combination effects. Sci Total Environ. 2022 Aug 1;832:155058.

63. Wang X, Ryu D, Houtkooper RH, Auwerx J. Antibiotic use and abuse: a threat to mitochondria and chloroplasts with impact on research, health, and environment. Bioessays. 2015 Oct;37(10):1045–53.

64. Zou M, Huang M, Zhang J, Chen R. Exploring the effects and mechanisms of organophosphorus pesticide exposure and hearing loss. Front Public Health. 2022;10:1001760.

65. Shenouda SM, Widlansky ME, Chen K, Xu G, Holbrook M, Tabit CE, et al. Altered mitochondrial dynamics contributes to endothelial dysfunction in diabetes mellitus. Circulation. 2011 Jul 26;124(4):444–53.

66. Frye RE, Lionnard L, Singh I, Karim MA, Chajra H, Frechet M, et al. Mitochondrial morphology is associated with respiratory chain uncoupling in autism spectrum disorder. Transl Psychiatry. 2021 Oct 13;11(1):527.

67. Rossignol DA, Genuis SJ, Frye RE. Environmental toxicants and autism spectrum disorders: a systematic review. Transl Psychiatry. 2014 Feb 11;4(2):e360.

68. Frye RE, Cakir J, Rose S, Palmer RF, Austin C, Curtin P. Physiological mediators of prenatal environmental influences in autism spectrum disorder. Bioessays. 2021 Sep;43(9):e2000307.

69. Frye RE, Cakir J, Rose S, Delhey L, Bennuri SC, Tippett M, et al. Prenatal air pollution influences neurodevelopment and behavior in autism spectrum disorder by modulating mitochondrial physiology. Mol Psychiatry. 2021 May;26(5):1561–77.

70. Frye RE, Cakir J, Rose S, Palmer RF, Austin C, Curtin P, et al. Mitochondria May Mediate Prenatal Environmental Influences in Autism Spectrum Disorder. J Pers Med. 2021 Mar 18;11(3):218.

71. Frye RE, Rose S, Wynne R, Bennuri SC, Blossom S, Gilbert KM, et al. Oxidative Stress Challenge Uncovers Trichloroacetaldehyde Hydrate-Induced Mitoplasticity in Autistic and Control Lymphoblastoid Cell Lines. Sci Rep. 2017 Jun 30;7(1):4478.

72. Brack W, Barcelo Culleres D, Boxall ABA, Budzinski H, Castiglioni S, Covaci A, et al. One planet: one health. A call to support the initiative on a global science-policy body on chemicals and waste. Environ Sci Eur. 2022;34(1):21.

73. Humboldt-Dachroeden S, Mantovani A. Assessing Environmental Factors within the One Health Approach. Medicina (Kaunas). 2021 Mar 5;57(3):240.

Legends to Figures

Figure 1.

Overview of the MITOMATICS workflow.

The main steps of automated analysis of mitochondrial morphology using the MITOMATICS workflow are presented. Cellular models are selected (MITOGATE) to assess the mitochondria-disrupting effects of single chemicals (*MitoCollapse*) or of molecules used in combination (*MitoCocktail*). Fluorescent images of live cultured cells with labeled mitochondria are captured and loaded into MitoRadar. The images are segmented and a total of 104 morphological and texture features are extracted for each frame. The values can be plotted for a particular cell or for all cells present in a given microscopic field, at the level of the whole mitochondrial population or for mitochondrial subnetworks. The software handles data analysis, statistics and visual exploration for instance in the form of radar plots. Reference condition is standardized by a blue circle for comparison with a different cellular state (lines with other colors). The basic steps of this wet-plus-dry pipeline are thus as follows: (i) Pre-acquisition steps: cell treatment including culture in 96-well plates, drug exposure and staining. (ii) Acquisition step: live-cell imaging (5 random fields/well) acquired on an Opera Phenix High-Content Screening system (or other imaging platform). (iii) Post-acquisition steps: fully automated image analysis by the MitoRadar software including image processing, AI-driven segmentation, parameter quantification, statistics, visual representation and scoring. Note that the Graphical Abstract shows a differently annotated

version of the pipeline: the step of cellular model selection corresponds to ‘Question to protocol’, pre-acquisition and acquisition steps are classed under the denomination ‘Cells to pixels’ and, lastly, post-acquisition steps are referred to as ‘Pixels to Data’ and ‘Data to Answer’.

Figure 2.

Implementation of the MITOPIX-DEV image dataset of BEAS-2B cells treated with mitochondrial pro-fission and hyper-fusion drugs.

BEAS-2B cells were treated with vehicle (0,5% DMSO), pro-fission drugs (20 µM CCCP, 1 µM Rotenone and 1 µM Antimycin A), and hyper-fusion drugs (50 µM MDIVI-1 and 10 µM M1) for 2h and stained with HOE (blue), CMG dye (green) and MTDR (purple) before confocal imaging (on the Opera Phenix HCS system). Images from the different fluorescent channels are presented separately or merged (overlay). Zoom-ins are shown. Scale bar = 10µm.

Figure 3.

Overwiew of the MitoRadar software.

(A) MitoRadar main page. The left panel allows users to manage data and launch image processing tasks while the center panel is dedicated to visualization (of both images and segmentation results). The right panel shows the descriptor values and their distribution for a single field or on the whole dataset. (B) MitoRadar basic features: a-Segmentation visualization panel (showing cells, nuclei, mitochondria and skeletons); b-Experimental data import module to link experimental data from the plates to the captured images; c-Advanced statistical panel to produce advanced statistical representations with PCA, LDA, Correlation, T-Test, SSMD and MitoRadar plots; d-Example of a 3D LDA plot produced with MitoRadar in-house statistical module. (C) The resulting data are plotted into MitoRadar charts, where the reference condition is standardized by a blue circle for comparison with another experimental condition of interest (orange line), such as chemical treatment or diseased status. Parameters can be

ranked in ascending order according to their SSMD values and they are colored in blue when the effect is diminished, brown when it is low and red when it is increased. Significant differences from basal for each experimental group are depicted by small (*: $p<0.05$), medium (**: $p<0.01$) or large (***: $p<0.001$) circles (Mann Whitney Test).

Figure 4.

Quantitative analysis of mitochondrial morphology in BEAS-2B cells treated with the mitochondrial uncoupler CCCP.

(A) Representative confocal microscopy images of BEAS-2B cells treated with 0,5% DMSO (vehicle, left panel) or 20µM CCCP (right panel) during 4h before mitochondrial staining (with MTDR). Scale bar = 10µm. (B) More than 4,000 CCCP-treated cells were analyzed using the MitoRadar software; the six different MitoRadar plots figure distribution of the normalized 104 morphometric features. The upper three MitoRadar plots correspond to computation for total mitochondria (*Mito*), clustered mitochondria (*Mitocluster*) or *Mitochondriome* (the full mitochondrial pool of a cell, considered as a single object), whereas the bottom three MitoRadar plots result from calculations of *Nuclear*, *Countershape* and cellular characteristics (*Cell*). Descriptors are colored in blue when the measured effect is diminished and in red when it is increased. Significant differences from basal (blue circle) for the CCCP-treated condition (orange line) are depicted by small (*: $p<0.05$), medium (**: $p<0.01$) or large (***: $p<0.001$) circles (Mann Whitney Test). Shown are representative data of n=5 independent experiments. (C) MitoRadar can calculate a MitoScore based on the deviation and number of affected parameters. Top 15 descriptors are listed. (D) Statistical analysis performed by MitoRadar. a- PCA plot on the first two components, with arrows indicating descriptor correlation with each axis; b- Box plot along the unique LDA axis; c- Violin plot showing a particular descriptor: Mito-roundness_mean, as an example.

Figure 5.

Quantitative analysis of mitochondrial morphology after acute exposure of human pulmonary cells to single pesticides (*MitoCollapse*).

(A) List of pesticides tested alone on BEAS-2B cells for 2h at different doses ranging from 10 to 500 µM, chemical category, threshold dose inferred by MitoRadar analysis and LD50 determined 24h post-treatment. (B) BEAS-2B cells were treated for 2h with vehicle (0,5% DMSO), 20µM of CCCP or 250µM of individual pesticides (FEN, PYRI, MEP, THI, AZO or PYRA). MitoRadar plots (morpho-phenotypic signatures) obtained after analysis by MitoRadar. For statistical analysis, a Mann-Whitney U test was used. Each MitoRadar plot results from analysis of around 20,000 cells and shown data are representative of 4 independent experiments. Note that when Mitoradar plots are computed with data obtained 2h post-treatment with 100µM of THI (**Fig. S6,** grey color), which is the calculated LD50/24h value for this pesticide, changes in parameters indicative of mitochondrial toxicity are already visible (with an increase in roundness_mean, circularity_mean, solidity_mean, compaction_mean and concomitant decrease in area_mean, axis_major_length_mean, axis_minor_length_mean, skel_length_mean). Complete single-compound dose–responses are shown in **Fig. S7**. (C) MitoScore for estimating treatment effect. Shown are the most affected parameters along a color-coded scale with explicit reference to one of the following five categories: *No effect, Limited / Substantial / Measurable* or *Large overall effect*. (D) Bidimensional representation of the established group into the new subspace generated by the first two LDA discriminant axis. Both LDA axis separate samples exposed to ETC complex I, II and III inhibitors and CCCP from the untreated ones.

Figure 6.

Quantitative analysis of mitochondrial morphology after acute exposure of human pulmonary cells to pesticide mixtures (*MitoCocktail*)

(A) List of pesticides tested alone on BEAS-2B cells for 4h at different doses ranging from 10 to 500 µM, chemical category, threshold dose inferred by MitoRadar analysis and LD50 determined 24h post-

treatment. Data shown are representative of at least 4 independent experiments with 4 replicates per experiment. (B) Table listing the main air-borne pesticides found in the five departments of region Occitanie (Southern France) and their relative percentage (according to real-world data produced by ATMO-Occitanie). The prominent pesticide (in red) detected in each of these five locations was tested at 5 doses ranging from 10 to 500 µM, the other pesticides in the mixture at the dose corresponding to their percentage in each region. The threshold dose inferred by MitoRadar and the LD50 are reported in the third and fourth column of the Table. (C) Representative confocal microscopy images of mitochondria (stained with MTDR) present in BEAS-2B cells after treatment with 0,5% DMSO (panel a), 10µM FOL (panel b), 50µM FOL (panel c) or with a mixture of pesticides found in the Aude department (one of the five departments of region Occitanie) with main pesticide (FOL) concentration set at 10 µM (panel d). (D) MitoRadar plots showing variations in mitochondrial parameters after treatment with vehicle (0,5% DMSO, blue circle), 10µM (orange), 50µM (green) or 100µM (red) of FOL alone (left MitoRadar) or by the mixture of pesticides found in Aude with the main pesticide (FOL) concentration set at 10, 50 or 100µM (respectively in orange, green and red in the right panel). (E) MitoScore for estimating treatment effect. Shown are the most affected parameters along a color-coded scale with explicit reference to one of the following five categories: *No effect*, *Limited / Substantial / Measurable* or *Large overall effect*.

Supplementary Information

Supplementary Figure 1 (Fig. S1).

MitoRadar segmentation module.

(A) Labelled nuclei, membranes and mitochondria are imaged and pictures are loaded into the MitoRadar software. The images are processed through successive segmentation, labelling and transformation steps. For the first segmentation step which consist in detecting cells and nuclei, MitoRadar uses deep learning. Image processing and morphometric measurements are fully automated and can be parallelized. (B) Descriptors pertaining to multiscale (wells /fields /cells / nuclei /

mitochondriome / countershape /clusters of mitochondria/ isolated mitochondria) and multidimensional analysis (n=104) for identification of complex phenotypes. (C) Segmentation step (detail). Tri-channel staining (a): cell membranes are labeled in green, nuclei in blue and mitochondria in purple. Cell label (b). Nuclei label (c). Clustered mitochondria label (d). Mitochondrial skeleton label (e). Isolated mitochondria label (f). Note that in our image analysis workflow, images were "down-sampled" only for the nuclei and cytoplasm channels to maximize segmentation efficacy and computational efficiency (these objects being large enough, this operation only minimally affects their definition). Mitochondrial segmentation was carried out at the maximum image resolution (i.e., images were processed at full resolution without any pre-processing step).

Supplementary Table 1 (Table S1).

List of descriptors, classification and definition.

Supplementary Figure 2 (Fig. S2).

Fluorescence imaging of eight human cell lines.

Representative confocal microscopy images of the following cell lines: BEAS-2B (non-tumorigenic lung epithelial cells), A549 (lung adenocarcinoma cells), RPE-1 (retinal pigment epithelial-1 cells), U2OS (osteosarcoma cells), Hs68 (foreskin fibroblasts), THLE-3 (liver epithelial cells), MDA-MB231 (triple-negative breast cancer cells) and HK-2 (kidney proximal tubule cells). Nuclei were labelled using Hoechst (blue; HOE), membranes with CellMask dye (green; CMG) and mitochondria with the mitochondria-specific dye MitoTracker Deep Red FM (purple; MTDR). Pictures were taken by live-cell confocal microscopy on the Opera Phenix® HCS system. Images from the different fluorescent channels are presented separately or merged (overlay). N=2 independent experiment with 10 replicates for each condition and more than 10,000 analyzed fields. Zoom-ins are shown. Scale bar = 10µm.

Supplementary Figure 3 (Fig. S3).

Treatment of different human cell lines with mitochondrial pro-fission and hyper-fusion drugs for implementation of the MITOPIX-DEV image dataset.

BEAS-2B, A549, RPE-1, U2OS, Hs68, THLE-3, MDA-MB231 and HK-2 cells were treated with vehicle (DMSO), pro-fission drugs (20 µM CCCP, 1 µM Rotenone and 1 µM Antimycin A), and hyper-fusion drugs (50 µM MDIVI-1 and 10 µM M1) for 2h and stained with HOE (blue), CMG dye and MTDR before confocal imaging (on the Opera Phenix® HCS System). Images from the different fluorescent channels were merged (overlay). Zoom-ins are presented. Scale bar = 10µm.

Supplementary Figure 4 (Fig. S4)

Overview of MitoRadar statistical analysis system (example of CCCP treatment).

(A) Summary of the SSMD based on comparison between control cells (0.5% DMSO, vehicle) and cells treated with a pro-fission drug (20 µM CCCP for 4h). This measure of the size effect is greater between both groups when the square is red, and smaller when the square is blue. (B) and (C) U- and p-value computations using Mann-Whitney test and T-test respectively, plus Benjamini-Hochberg correction. When the difference between the compared groups is statistically significant for a given variable, the squares are labeled in dark green (see for instance Mito_roundness_mean), whereas when the differences are not significant, the squares are labeled in grey (see for instance the whole set of nuclear parameters). (D) Hierarchical clustering of the computed parameters. (E) Correlation distance map showing the dependence between descriptors. Detailed view of the correlation of descriptors along each axis for PCA (F) and LDA (G).

Supplementary Figure 5 (Fig. S5)

MitoRadar analytical platform with advanced statistics.

(A) MitoRadar plots showing features associated with nuclei, countershape and cells, after 2h exposure to 250µM of pesticides (FEN in red, PYRI in pink, MEP in violet, THI in grey, AZO in orange and PYRA in brown), 20 µM CCCP (in green) or 0,5% DMSO (blue circle as a reference). (B) Correlation distance map showing dependence between descriptors. (C) SSMD summary showing size effect. (D) U-values computations using Mann-Whitney test and significance level after Benjamini-Hochberg correction.

Supplementary Figure 6 (Fig. S6)

Quantitative analysis of mitochondrial morphology after acute exposure of human pulmonary cells to 100µM of single pesticides.

BEAS-2B cells were treated for 2h with vehicle (0,5% DMSO), 20µM of CCCP or 100µM of individual pesticides (FEN, PYRI, MEP, THI, AZO or PYRA). MitoRadar plots (morpho-phenotypic signatures) obtained after analysis by MitoRadar. For statistical analysis, a Mann-Whitney U-test was used. Each MitoRadar plot results from analysis of around 20,000 cells and shown data are representative of 4 independent experiments.

Supplementary Figure 7 (Fig. S7)

Quantitative analysis of mitochondrial morphology after acute exposure of human pulmonary cells to 10-500µM of single pesticides (dose-reponses).

BEAS-2B cells were treated for 2h with vehicle (0,5% DMSO, blue circle), 20µM of CCCP (pink broken line) or with 10µM (orange), 50 µM (purple), 100µM (green), 250µM (red), or 500µM (brown) of individual pesticides (FEN, PYRI, MEP, THI, AZO or PYRA). MitoRadar plots (morpho-phenotypic signatures) obtained after analysis by MitoRadar. For statistical analysis, a Mann-Whitney U-test was used. Each MitoRadar plot results from analysis of around 20,000 cells and shown data are representative of 4 independent experiments.

Figure 1

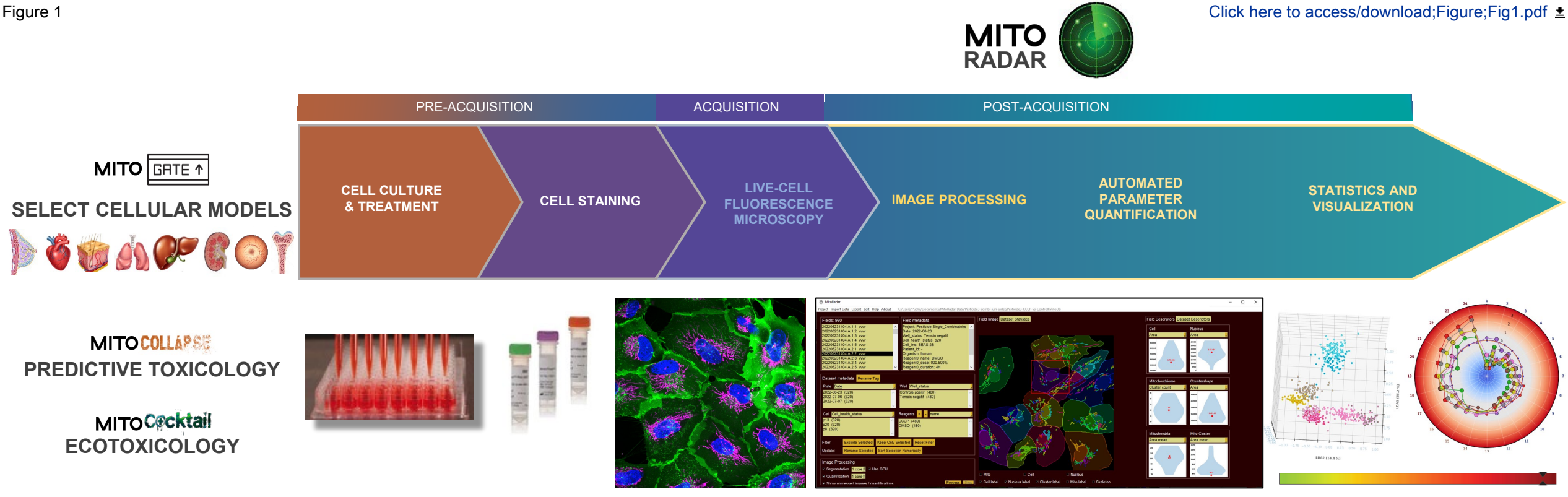

Figure 2

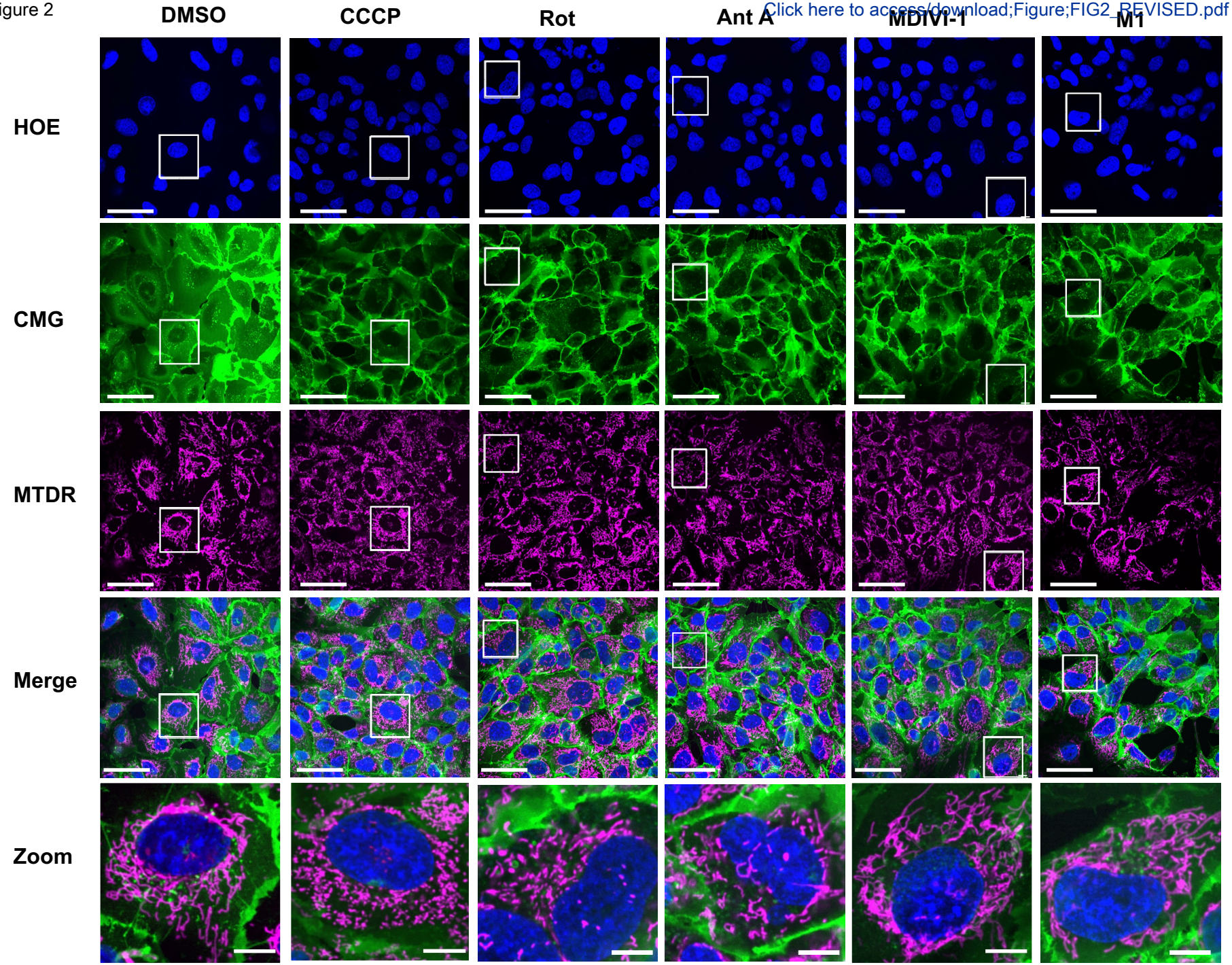

Figure 3

A

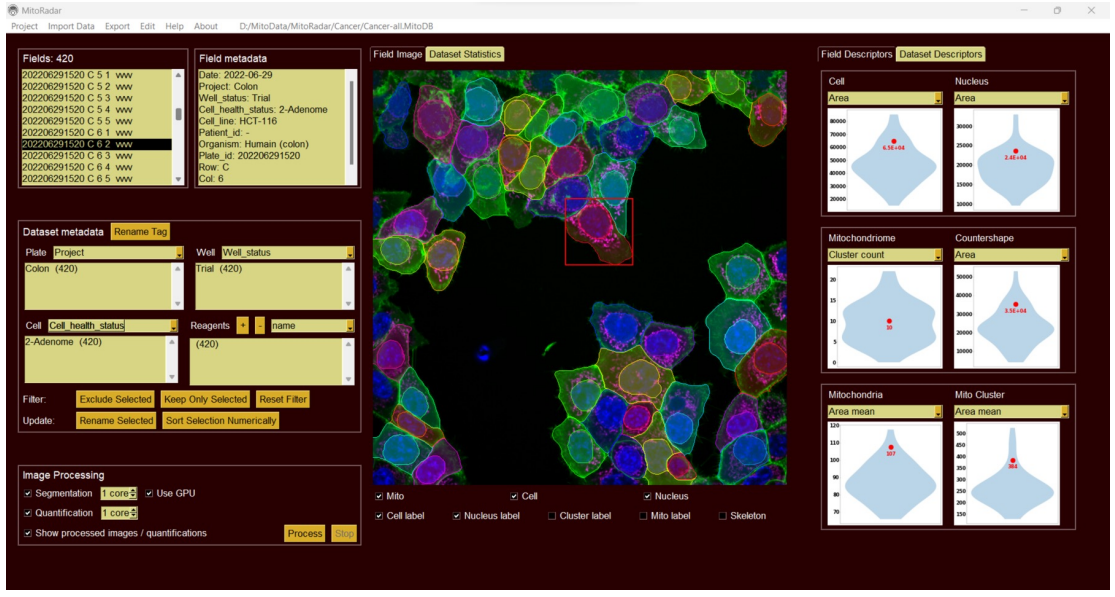

B

a

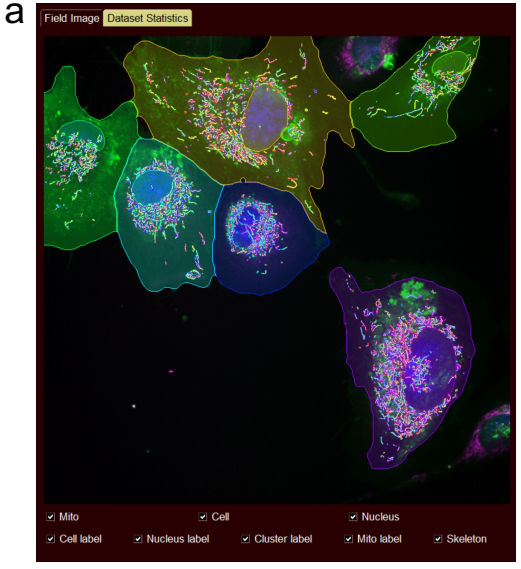

b

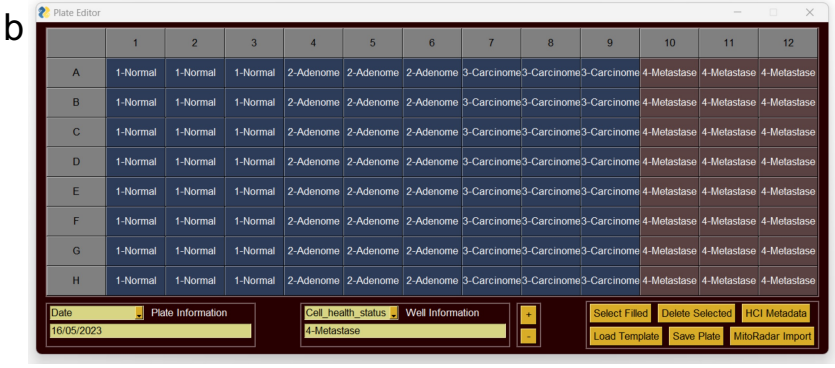

c

C

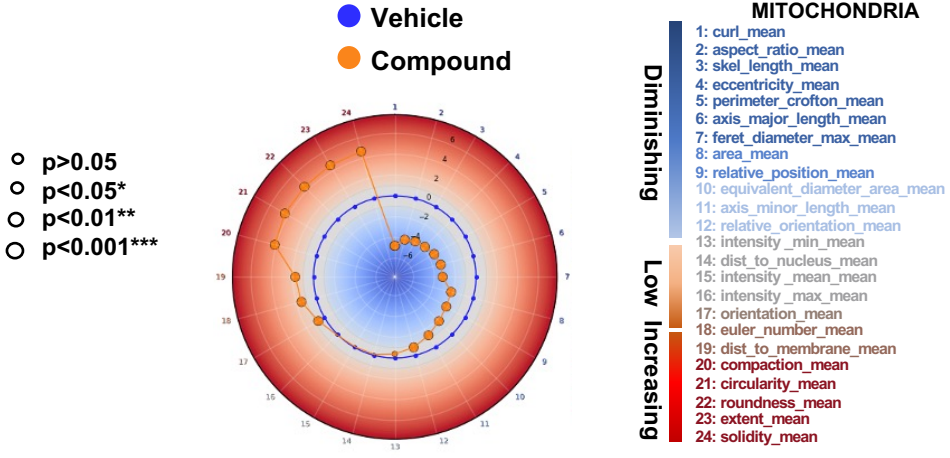

d

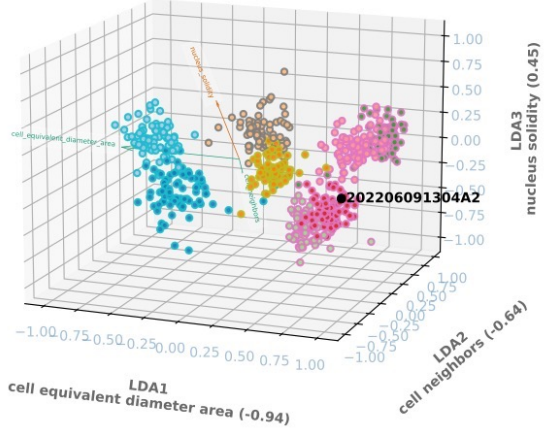

Figure 4

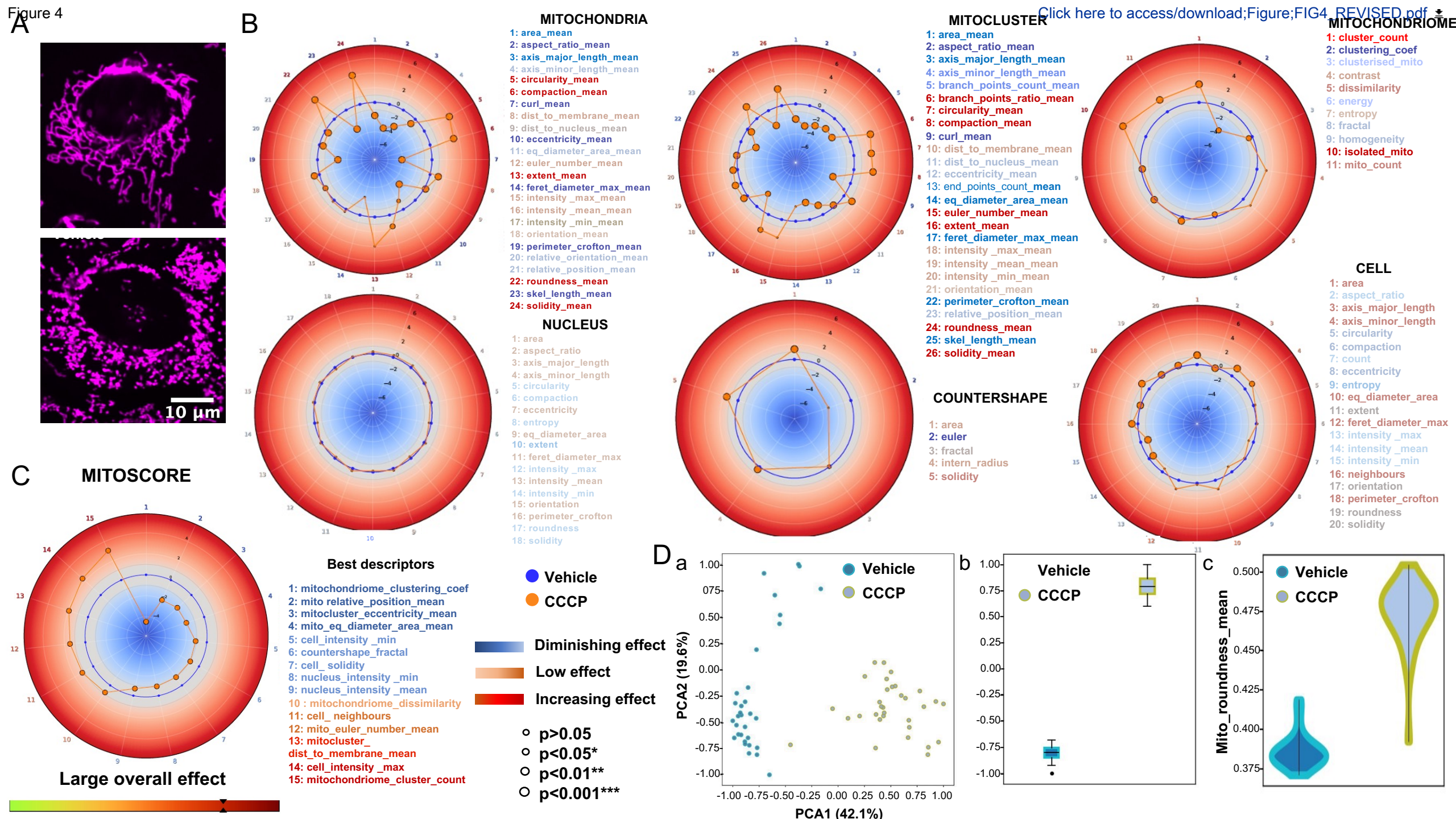

Figure 5

A

PESTICIDES	CATEGORY	THRESHOLD DOSE	LD50
FENPYROXIMATE	ACARICIDE	50µM	>500µM
PYRIDABEN	ACARICIDE	50µM	>500µM
MEPRONIL	FONGICIDE	50µM	≥ 500µM
THIFLUZAMIDE	FONGICIDE	10µM	100µM
AZOXYSTROBIN	FONGICIDE	100µM	≥ 500µM
PYRACLOSTROBIN	FONGICIDE	10µM	>500µM

C

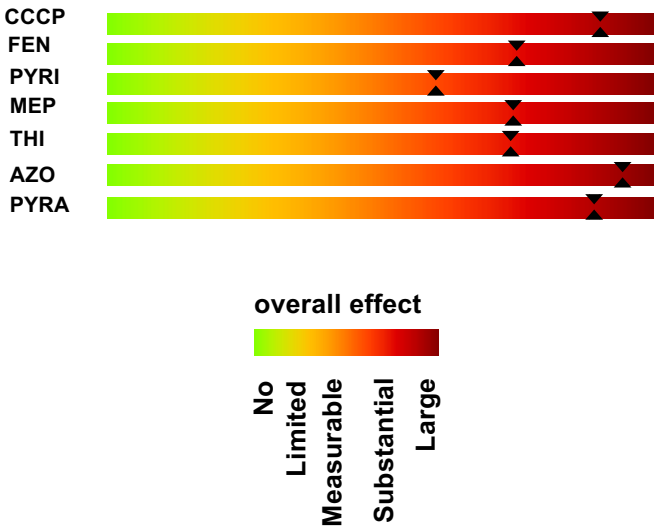

D

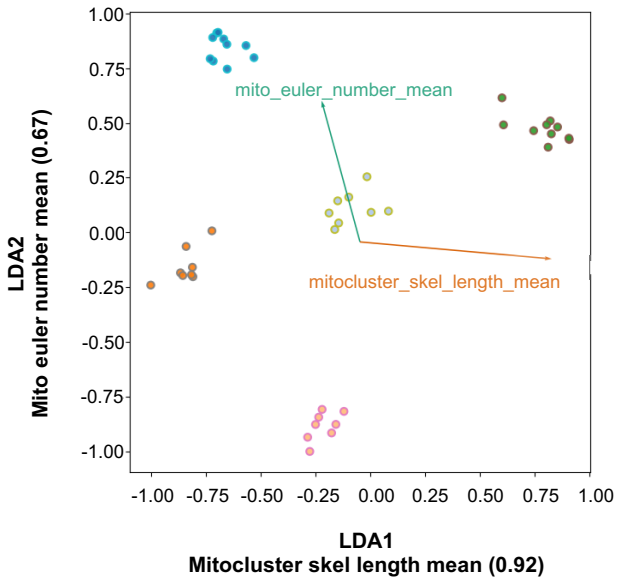

B

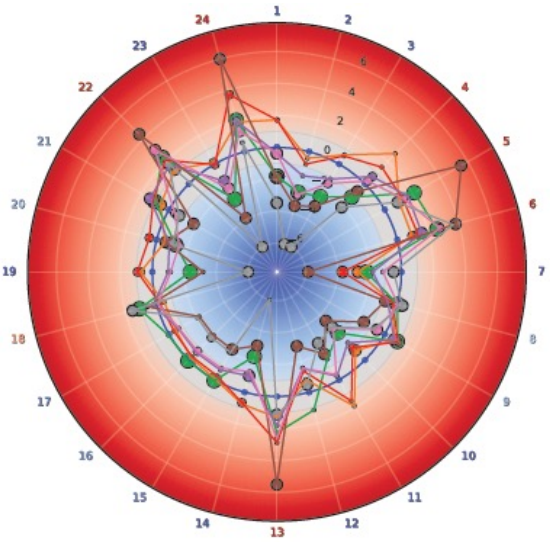

Vehicle
CCCP
FEN
PYRI
MEP
THI
AZO
PYRA

Diminishing effect
Low effect
Increasing effect

MITOCHONDRIA

1: area_mean
2: aspect_ratio_mean
3: axis_major_length_mean
4: axis_minor_length_mean
5: circularity_mean
6: compaction_mean
7: curl_mean
8: dist_to_membrane_mean
9: dist_to_nucleus_mean
10: eccentricity_mean
11: equivalent_diameter_area_mean
12: euler_number_mean
13: extent_mean
14: feret_diameter_max_mean
15: intensity _max_mean
16: intensity _mean_mean
17: intensity _min_mean
18: orientation_mean
19: perimeter_crofton_mean
20: relative_orientation_mean
21: relative_position_mean
22: roundness_mean
23: skel_length_mean
24: solidity_mean

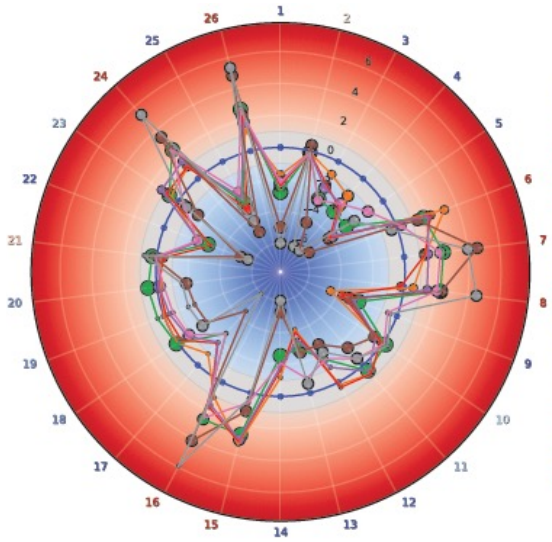

MITOCLUSTER

1: area_mean
2: aspect_ratio_mean
3: axis_major_length_mean
4: axis_minor_length_mean
5: branch_points_count_mean
6: branch_points_ratio_mean
7: circularity_mean
8: compaction_mean
9: curl_mean
10: dist_to_membrane_mean
11: dist_to_nucleus_mean
12: eccentricity_mean
13: end_points_count_mean
14: equivalent_diameter_area_mean
15: euler_number_mean
16: extent_mean
17: feret_diameter_max_mean
18: intensity _max_mean
19: intensity _mean_mean
20: intensity _min_mean
21: orientation_mean
22: perimeter_crofton_mean
23: relative_position_mean
24: roundness_mean
25: skel_length_mean
26: solidity_mean

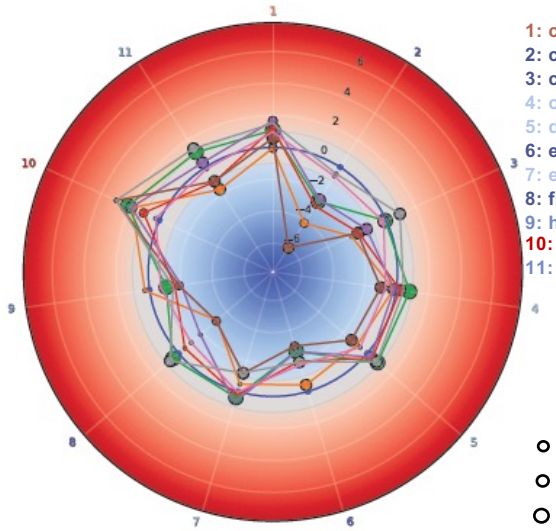

MIITOCHONDRIOME

1: cluster_count
2: clustering_coef
3: clusterised_mito
4: contrast
5: dissimilarity
6: energy
7: entropy
8: fractal
9: homogeneity
10: isolated_mito
11: mito_count

- p>0.05
- p<0.05*
- p<0.01**
- p<0.001***

Figure 6

A

PESTICIDES	CATEGORY	THRESHOLD DOSE	LD50
FOLPEL	FONGICIDE	50µM	150µM
PENDIMATHALINE	HERBICIDE	250µM	>500µM
CHLORPYRIPHOS	FONGICIDE	50µM	100µM
LINDANE	INSECTICIDE	500µM	500µM
CYPRODINIL	FONGICIDE	100µM	75µM

B

DEPARTMENT	PESTICIDE COMBINATION	PERCENTAGE IN MIXTURE	THRESHOLD DOSE	LD50
TARN ET GARONNE	PENDIMATHALINE FOLPEL LINDANE CYPRODINIL	83% 8% 6,5% 2,2%	50µM 4,8µM 1,3µM 3,9µM	100µM 9,6µM 2,6µM 7,8µM
PYRENEES-ORIENTALES	FOLPEL PENDIMATHALINE CHLORPYRIPHOS CYPRODINIL	88% 4% 4% 4%	10µM 0,47µM 0,47µM 0,47µM	10µM 0,47µM 0,47µM 0,47µM
LAURAGAIS	PENDIMATHALINE FOLPEL LINDANE	78% 20% 1,8%	50µM 13,3µM 1,2µM	100µM 27µM 2,4µM
AUDE	FOLPEL PENDIMATHALINE CHLORPYRIPHOS LINDANE	97% 1,1% 0,8% 1,5%	10µM 0,11µM 0,15µM 0,08µM	10µM 0,11µM 0,15µM 0,08µM
GARD	FOLPEL PENDIMATHALINE CHLORPYRIPHOS	93% 1,5% 5%	10µM 0,2µM 0,54µM	10µM 0,2µM 0,54µM

C

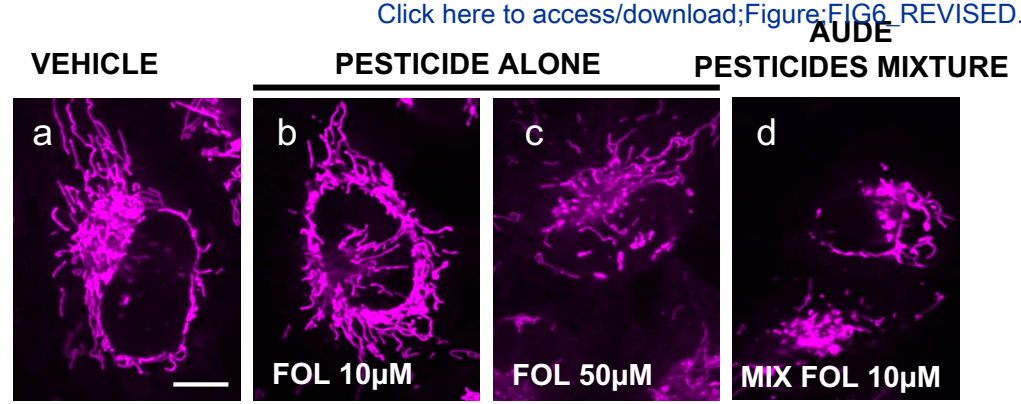

D

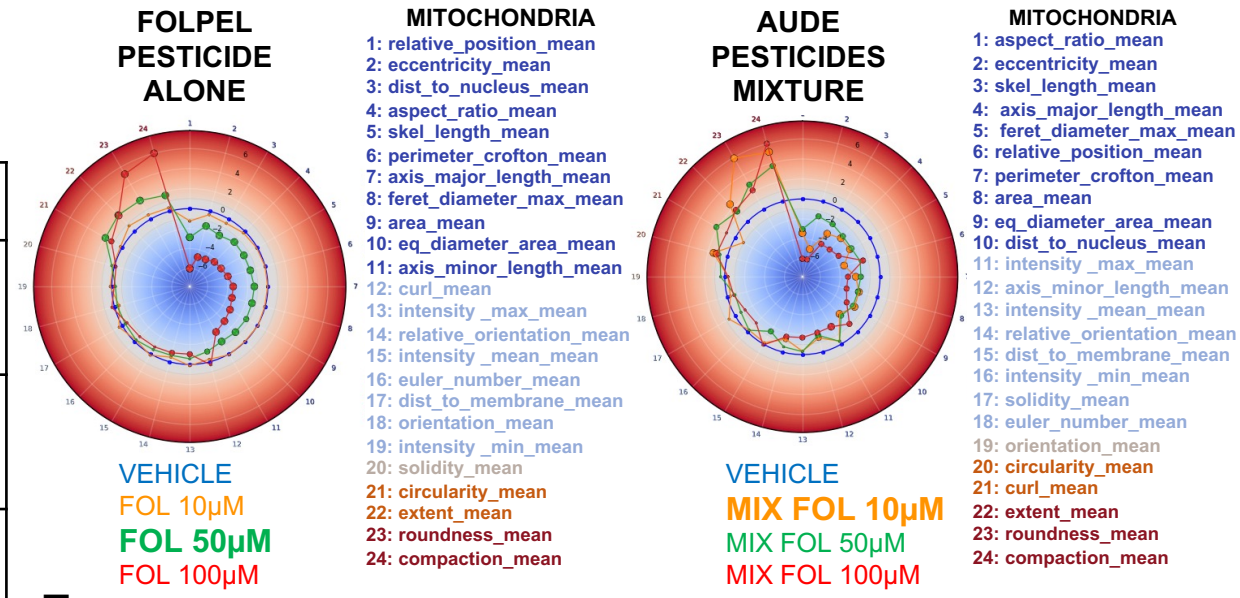

E

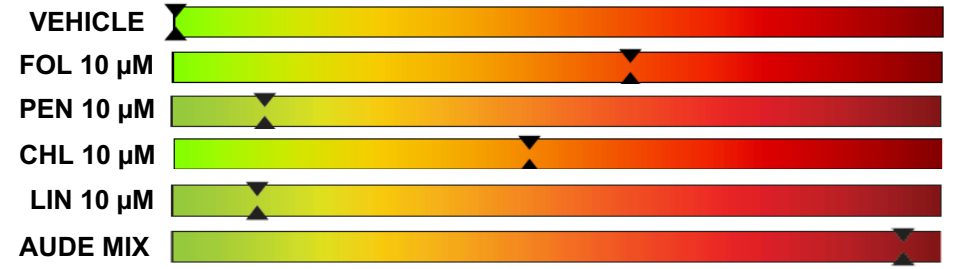

Conflict of Interest

Declarations of interest: none.

Sophie Charrasse: Data curation; formal analysis; investigation; visualization; methodology; writing – review and editing.

Charlotte Saint-Omer: Data curation; formal analysis; investigation; visualization; methodology.

Benoît Bordignon: Data curation; formal analysis; investigation; visualization; methodology.

Manuela Pastore : Data curation; software; formal analysis; investigation; visualization; methodology; writing – review and editing.

Richard E. Frye : Resources; data curation; methodology; writing – review and editing.

Titouan Poquillon : Data curation; software; formal analysis; investigation; visualization; methodology; writing – review and editing.

Victor Racine : Data curation; software; formal analysis; investigation; visualization; methodology; writing – review and editing.

Christelle Reynes : Data curation; software; formal analysis; investigation; visualization; methodology; writing – review and editing.

Abdel Aouacheria: Conceptualization; data curation; formal analysis; supervision; funding acquisition; investigation; visualization; writing – original draft; project administration; writing – review and editing.

Figure S1

Figure S2

Figure S3

Figure S4

Figure S5

Figure S6

Figure S7